

Prevention is better than cure? Feedback from high specific energy winds in cosmological simulations with ARKENSTONE

Jake S. Bennett¹,^{*} Matthew C. Smith²,² Drummond B. Fielding^{3,5}, Greg L. Bryan^{4,5}, Chang-Goo Kim⁶,⁶ Volker Springel² and Lars Hernquist¹

¹Center for Astrophysics | Harvard & Smithsonian, 60 Garden Street, Cambridge, MA 02138, USA

²Max-Planck-Institut für Astrophysik, Karl-Schwarzschild-Str. 1, D-85748, Garching, Germany

³Department of Astronomy, Cornell University, Ithaca, NY 14853, USA

⁴Department of Astronomy, Columbia University, 550 West 120th Street, New York, NY 10027, USA

⁵Center for Computational Astrophysics, Flatiron Institute, 162 5th Avenue, New York, NY 10010, USA

⁶Department of Astrophysical Sciences, Princeton University, 4 Ivy Lane, Princeton, NJ 08544, USA

MNRAS, submitted

ABSTRACT

We deploy the new ARKENSTONE galactic wind model in cosmological simulations for the first time, allowing us to robustly resolve the evolution and impact of high specific energy winds. In a $(25 h^{-1} \text{ Mpc})^3$ box we perform a set of numerical experiments that systematically vary the mass and energy loadings of such winds, finding that their energy content is the key parameter controlling the stellar to dark matter mass ratio. Increasing the mass loading, at fixed energy, actually results in mildly *enhanced* star formation, counter to prevailing wisdom but in agreement with recent analytic models. Of the simple parametrisations that we test, we find that an energy loading that scales inversely with halo mass best matches a wide range of observations and can do so with mass loadings drastically lower than those in most previous cosmological simulations. In this scenario, much less material is ejected from the interstellar medium. Instead, winds both heat gas in the circumgalactic medium, slowing infall onto the galaxy, and also drive shocks beyond the virial radius, preventing accretion onto the halo in the first place. We have not yet tied the mass and energy loadings to high-resolution simulations (a key goal of the Learning the Universe collaboration); however, we can already report that a much lower fraction of the available supernova energy is needed in preventative galaxy regulation than required by ejective wind feedback models such as IllustrisTNG.

Key words: methods: numerical – galaxies: formation – galaxies: evolution – hydrodynamics

1 INTRODUCTION

To first order, in the Λ CDM cosmological model, galaxy formation just involves the gravitational collapse of dark matter (DM) hierarchically into DM haloes, with subsequent condensation of baryons into their gravitational potential followed by the formation of stars (Rees & Ostriker 1977; Silk 1977; White & Rees 1978; White & Frenk 1991). However, reality is likely much more complicated, due to the complex interplay of accretion onto galaxies and their interstellar medium (ISM), along with outflows of mass and energy driven by feedback processes. This feedback is thought to be essential, as simulations that do not include it significantly overproduce stars, leading to very massive, compact galaxies (e.g. Navarro & White 1994; Navarro et al. 1995).

Feedback is generally believed to come from two primary sources: black holes (BHs) and stars (see e.g. Heckman & Best 2023). In lower mass haloes, below approximately $10^{12} M_{\odot}$, the dominant effect is thought to be stellar feedback, from stellar winds, radiation, and supernovae, while massive galaxies are regulated by BH feedback

(see e.g. Somerville & Davé 2015). At all mass scales, regulation of star formation occurs ultimately by reducing the efficiency of the conversion of gas into stars. On small spatial scales, energy injection in the galaxy causes heating and drives turbulence in the ISM, disrupting star formation (e.g., Ostriker et al. 2010; Hopkins et al. 2011; Faucher-Giguère et al. 2013; Krumholz et al. 2018; Ostriker & Kim 2022). The key to the long-term regulation of star formation however lies in the larger scale baryon cycle, in which galactic winds play a key role (e.g., Strickland & Stevens 2000; Oppenheimer & Davé 2008; Hopkins et al. 2012; Anglés-Alcázar et al. 2017; Wright et al. 2024).

Winds can act as feedback in two ways. They can remove material from the ISM, reducing the amount of gas available to form stars and carrying mass and metals out into the circumgalactic medium (CGM) – *ejective* feedback. They can also slow or stop gas from accreting onto the galaxy to replenish the fuel for star formation, via the injection of energy into the CGM (or beyond) – *preventative* feedback. We can characterise winds with two key parameters: the mass loading (η_M , the ratio of the wind mass flux and the star formation rate) and the energy loading (η_E , the ratio of the wind energy flux and the rate at which energy is released during star formation

* E-mail: jake.bennett@cfa.harvard.edu

and stellar evolution). We will discuss these parameters extensively in this work.

A wealth of observational evidence exists for outflowing material around many galaxies (see [Rupke 2018](#), for a review), including from spectroscopic detections of outflows themselves and metal pollution of the CGM at large distances from the central galaxy (e.g. [Prochaska et al. 2017](#); [Guo et al. 2020](#); [Zabl et al. 2021](#)). These outflows are ubiquitously found to be multiphase, with molecular, neutral and ionised gas found to co-exist using probes across the electromagnetic spectrum (e.g. [Rupke 2018](#); [Thompson & Heckman 2024](#)). Despite the widespread detection of outflows around galaxies, estimating the mass and energy loading values is very difficult – especially in the hottest gas phases. Where such data exists, mass fluxes are reliably found to be low relative to the star formation rate (e.g. [McQuinn et al. 2019](#); [Concas et al. 2022](#); [Marasco et al. 2022](#); [Kado-Fong et al. 2024](#)) and the energy flux is found to be comparable to the energy injected by supernovae (e.g. [Strickland & Heckman 2009](#)).

Such multiphase winds have emerged naturally in high resolution (\sim pc) simulations that include most of the physics thought to be important to star formation and stellar feedback using small (\sim kpc) patches of the ISM (e.g. [Kim & Ostriker 2018](#); [Kim et al. 2020a](#); [Kannan et al. 2020](#); [Rathjen et al. 2023](#)) and low mass galaxies (e.g. [Smith et al. 2018, 2021](#); [Hu 2019](#); [Steinwandel et al. 2024b](#)). A recent consensus of such detailed simulations is that not all wind phases are created equally – a hot, fast phase ($\gtrsim 10^6$ K) carries most of the energy in the wind, and a slower, cooler phase ($\lesssim 10^4$ K) carries most of the mass ([Fielding et al. 2018](#); [Kim et al. 2020a](#); [Li & Bryan 2020](#)).

Recent analytic and semi-analytic models incorporating energy injection and heating of the CGM have highlighted the importance of the hot wind phase, in the form of high specific energy winds ([Carr et al. 2023](#); [Pandya et al. 2023](#); [Voit et al. 2024a,b](#)). In particular, the regulator model of [Carr et al. \(2023\)](#) suggested that the amount of energy carried by a hot wind is more important in regulating star formation than the amount of mass comprising the wind. However, due to the large spatial extent and timescales involved, following the evolution of such a wind after it has launched, and the long-term effect on its host galaxy (\sim Mpc), has yet to be done in full cosmological simulations.

To study the impact of energy and mass loadings for a statistically large sample of galaxies, we require cosmological box simulations (\gg Mpc). However, the resolution of such simulations precludes the *ab initio* formation of galactic winds. Primarily this is due to under-resolving the ISM, where energy injected into dense gas is typically radiated away unphysically rapidly before an outflow can be launched. Subgrid models used for stellar feedback generally circumvent this in one of two ways. The first is by overpowering cooling through the rare, stochastic injection of large amounts of energy representing multiple supernovae events (e.g. [Dalla Vecchia & Schaye 2012](#); [Schaye et al. 2015](#); [McCarthy et al. 2017](#)). However, low resolution in the ISM combined with discrete injections of energy (e.g. from supernovae) lead to a wind energy injection rate that is dependent on mass resolution – trying to power a high specific energy wind with coarse resolution wind particles results in an artificially bursty energy injection. The second is through bypassing the ISM entirely. Many models use hydrodynamically decoupled wind particles, launched from the ISM, that typically recouple in the inner CGM and launch a wind from there (e.g. [Springel & Hernquist 2003](#); [Vogelsberger et al. 2013](#); [Davé et al. 2016, 2019](#); [Henden et al. 2018](#); [Pillepich et al. 2018a](#)). In most simulations, an effective equation of state model (e.g. [Springel & Hernquist 2003](#); [Schaye & Dalla Vecchia 2008](#)) is then used to capture the unresolved small-scale heating and turbulence of the ISM. Most subgrid models launch a single wind phase,

with the same launch velocity and mass loading (e.g. [Vogelsberger et al. 2013](#); [Pillepich et al. 2018a](#)), though several also add a thermal component to either all wind particles ([Pillepich et al. 2018a](#)) or a fraction of particles ([Davé et al. 2016, 2019](#)) to mimic the impact of hot wind material. No cosmological simulation reliably resolves the interaction between hot and cold phases of material in a wind, which would likely require sub-solar mass resolution (e.g., [McCourt et al. 2018](#); [Gronke & Oh 2020](#); [Abruzzo et al. 2024](#)).

Most modern cosmological box simulations tune the parameters of their models to match particular observables (e.g. the stellar mass – halo mass relation). After this process, the mass and energy loading factors for stellar feedback in most cosmological simulations are typically much higher than what is measured in resolved ISM simulations (e.g. [Li & Bryan 2020](#)). Different simulations can have drastically different predictions for secondary properties of galaxies, most notably in the CGM ([Fielding et al. 2017](#); [Davies et al. 2019, 2020](#); [Fielding et al. 2020](#); [Kelly et al. 2022](#); [Ayromlou et al. 2023](#); [Wright et al. 2024](#)). Resolution also affects the properties of the simulated CGM, further complicating the matter, though some recent progress has been made using simulations that specifically focus computational resources on the CGM (e.g. [Hummels et al. 2019](#); [Peeples et al. 2019](#); [van de Voort et al. 2019](#); [Suresh et al. 2019](#); [Bennett & Sijacki 2020](#); [Ramesh & Nelson 2024](#)). How much of the discrepancies between simulations are due to the numerical implementation of subgrid models is unclear; until now it has not been possible to study the regulatory effect of high specific energy, low mass winds on a large population of galaxies.

Simulating high specific energy winds is challenging in cosmological simulations (see section 2 of [Smith et al. 2024a](#), for a detailed description). Hot, fast winds with low mass fluxes have lower densities, leading to coarser spatial resolution in a Lagrangian code (or with a quasi-Lagrangian refinement strategy in an Eulerian scheme, as is typical in cosmological volumes). Even with the highest mass resolution of current cosmological box simulations ($\sim 10^5 M_\odot$) such a wind can become completely unresolved, with single resolution elements being larger than the galaxy launching them (see fig. 1 of [Smith et al. 2024a](#)).

To address these issues, ARKENSTONE a new subgrid model for multiphase winds, was developed ([Smith et al. 2024a,b](#)). The full model launches winds containing both a high specific energy component (ARKENSTONE-HOT, [Smith et al. 2024a](#), henceforth S24) and an unresolved cold cloud component (ARKENSTONE-COLD, [Smith et al. 2024b](#)), each with their own mass and energy loadings. With the full model, we can explore a huge area of previously unexplored parameter space to investigate the balance between ejective and preventative feedback in galaxy formation. The ultimate aim is to use parameters calibrated in highly resolved ISM simulations as inputs to the ARKENSTONE model, to remove the calibration step common to most cosmological simulations (e.g. [Kim et al. 2020b](#)) – key aims of the SMAUG¹ (Simulating Multiscale Astrophysics to Understand Galaxies) and Learning the Universe² collaborations.

In this first paper applying the ARKENSTONE model to cosmological simulations we focus only on the hot component of winds, allowing us to study galaxy formation in a regime where preventative feedback dominates and little mass is ejected from the ISM. We vary the key parameters of these hot winds – mass and energy loadings –

¹ <https://www.simonsfoundation.org/flatiron/center-for-computational-astrophysics/galaxy-formation/smaug/>

² <http://learning-the-universe.org>

to study how the properties of the galaxy population respond. The paper is structured as follows: In Section 2 we describe in detail the ARKENSTONE model and the simulations in this paper. Sections 3.1 and 3.2 show properties of the galaxies and their gaseous haloes in our simulations at $z = 0$. Section 3.4 then looks at a subset of these quantities at $z = 2$ to demonstrate how ARKENSTONE regulates star formation through preventative, rather than ejective feedback. We look at the redshift evolution of star formation in Section 3.5, discuss comparisons to recent analytic, semi-analytic and simulation work in Section 4, and summarise our results in Section 5.

2 METHODS

2.1 Simulation set-up

The simulations in this paper use AREPO (Springel 2010), a cosmological code that incorporates gravity using a TreePM scheme and solves the equations of hydrodynamics on a quasi-Lagrangian, unstructured, moving Voronoi mesh, where mesh generating points move with the fluid velocity (with small corrections in selected cells to promote a regular mesh geometry). In AREPO, a default refinement scheme keeps gas cells within a factor of two of a given mass resolution by merging and splitting cells, as non-zero mass fluxes between cells can lead to fluctuations in cell masses. In ARKENSTONE, this is supplemented with an additional refinement scheme, as described in Section 2.4.

We perform a number of numerical experiments using ARKENSTONE-HOT in cosmological box simulations to explore the ability of high specific energy winds to act as preventative feedback. This is motivated by recent analytic and semi-analytic works suggesting an important role for such winds (Carr et al. 2023; Pandya et al. 2023; Voit et al. 2024a,b), but until now such a scenario has not been investigated in full cosmological hydrodynamical simulations. To study the impact of these winds, we vary the input parameters of the wind – specifically the mass and energy loadings – and investigate changes in the population-level properties of galaxies due to these variations. We emphasise that we have *not* calibrated the input parameters of the ARKENSTONE wind model in this work to match observations, we simply test the impact of certain parameter choices motivated by analytic and semi-analytic modelling, and high resolution ISM simulations.

As a comparison we present our results alongside those from the existing TNG model (which is calibrated to match certain observations), described below, which uses a much more ejective feedback model to successfully reproduce a whole host of galaxy observables. Where available, we also show observationally inferred data for galaxy properties. We note, however, that in this work we do not forward model our simulation predictions into the observational space, so direct comparisons with observational data should be done with caution.

The cosmological simulations in this work all use the same periodic box with a comoving side length of 36.9 Mpc. The box has a cosmology consistent with Planck’s 2015 results (Planck Collaboration et al. 2016): $\Omega_m = 0.3089$, $\Omega_\Lambda = 0.6911$, $\Omega_b = 0.0486$, $h = 0.6774$, $\sigma_8 = 0.8159$, $n_s = 0.9667$. Initial conditions were generated with the N-GENIC code (Springel et al. 2005; Springel 2015).

The box contains 512^3 dark matter particles and is initialised with the same number of gas cells, corresponding to a dark matter particle mass of $1.24 \times 10^7 M_\odot$ and a base resolution baryon mass of $2.32 \times 10^6 M_\odot$. Gravitational softening lengths for DM and stars

are 1.48 ckpc at $z > 1$, and 0.74 pkpc at $z \leq 1$. Gas softenings are adaptive, but have a minimum of 0.37 pkpc. This is typical of large-scale cosmological boxes like TNG100 (Springel et al. 2018; Nelson et al. 2018; Naiman et al. 2018; Marinacci et al. 2018; Pillepich et al. 2018b), EAGLE (Schaye et al. 2015; Crain et al. 2015), Horizon-AGN (Dubois et al. 2014), and SIMBA (Davé et al. 2019).

2.2 Galaxy formation model

Aside from the supernova-driven wind model, all simulations presented in this paper share the same physical model in every respect. This model is the same as the fiducial IllustrisTNG simulations, with the exception of magnetohydrodynamics (MHD), that we omit in this work³. We will describe the ARKENSTONE wind model in Sections 2.3 and 2.4, and the TNG wind model in Section 2.5. First, however, we describe the physics common to all simulations (see Vogelsberger et al. 2013; Weinberger et al. 2017; Pillepich et al. 2018a, for further details).

We include radiative cooling in the same way as the original Illustris simulation and TNG (for full details, see Vogelsberger et al. 2013). Gas cooling occurs in the presence of a spatially uniform, time-varying ionising UV background, with corrections for self-shielding in dense gas (Faucher-Giguère et al. 2009; Rahmati et al. 2013). The background radiation field is also locally modified by a contribution from nearby AGN (see Vogelsberger et al. 2013). Cooling is included for both primordial species (Cen 1992; Katz et al. 1996), and metals (included using tabulated values as a function of metallicity, density, temperature, and redshift, Smith et al. 2008; Wiersma et al. 2009).

The resolution achievable in the ISM within cosmological simulations precludes the explicit modelling of a multiphase medium. We therefore adopt a modified version of the effective equation of state (eEoS) model from Springel & Hernquist (2003) to capture the unresolved, local effects of feedback on the ISM. The modifications are the same as in Illustris and TNG (see Vogelsberger et al. 2013); to avoid overpressurising the ISM, we interpolate between the Springel & Hernquist (2003) eEoS and an isothermal EoS at 10^4 K, with a fraction of 0.3 contributed by the eEoS. All gas cells with a number density above a threshold $n_{H,0} \approx 0.1 \text{ cm}^{-3}$ become part of the eEoS. Metal enrichment occurs via the release of metals to neighbouring cells of star particles in the ISM, at a rate determined by stellar population ages (see Vogelsberger et al. 2013; Pillepich et al. 2018a).

We use the model for BH seeding, growth, and feedback from TNG unchanged (for full details, see Weinberger et al. 2017). BHs of mass $1.18 \times 10^6 M_\odot$ are seeded into haloes with a mass larger than $7.38 \times 10^{10} M_\odot$. They can grow via mergers, or through accreting gas at the Eddington-capped Bondi accretion rate (Hoyle & Lyttleton 1939; Bondi & Hoyle 1944; Bondi 1952). Feedback energy is injected as a thermal dump local to the BH at high accretion rates, and as kinetic ‘kicks’ in the low accretion rate regime, motivated by expectations for quasar-driven winds and advection-dominated inflow-outflow solution (ADIOS) winds, respectively. We note that the interaction between ARKENSTONE and the TNG BH accretion and feedback models will not be trivial, as the parameters of the BH model were calibrated alongside the original TNG wind model. The different stellar feedback prescriptions may therefore affect BH growth differently. For this reason we restrict the bulk of our analysis in this paper to halo masses for which black holes do not strongly affect the evolution of galaxies (below halo masses of $\sim 10^{12.5} M_\odot$).

³ The ARKENSTONE model is compatible with MHD, but for simplicity in these first simulations we use hydrodynamics.

and we defer a detailed study of the combined feedback effect to future work.

We also use a friends-of-friends algorithm (Davis et al. 1985) and the SUBFIND halo finder (Springel et al. 2001; Dolag et al. 2009) to identify haloes and galaxies on-the-fly.

Finally, we emphasise that the parameters of the TNG model (with the inclusion of its wind model) were calibrated to reproduce a set of observables, namely the SFR density as a function of z , the galaxy stellar mass function (SMF), the stellar mass to halo mass relation (SMHM), the BH mass to stellar mass relation, halo gas fractions, and galaxy stellar sizes. As of yet, we have not undertaken a similar calibration with ARKENSTONE. In this paper we show a set of numerical experiments showing the impact of changes in mass and energy loadings. A full flagship cosmological simulation, with parameters either calibrated or informed by idealised high-resolution ISM simulations, will be presented in a future work.

2.3 ARKENSTONE

ARKENSTONE is a framework for launching multiphase winds in cosmological simulations. It uses hydrodynamically decoupled wind particles to source a wind just outside the ISM, as the complex interaction between winds and the ISM is largely unresolved in coarse resolution cosmological simulations (as described in Section 1). The use of hydrodynamically decoupled wind particles has the added benefit of allowing us to control the properties of galactic winds more closely, so we can more easily investigate the impact of these properties on the CGM. We note that ARKENSTONE uses a completely independent wind particle implementation to that used in TNG, and is fully compatible with all other TNG physics.

In this work we only employ the ARKENSTONE-HOT framework, which launches high specific energy winds (described in S24), and do not include the impact of cold clouds as further described in Smith et al. (2024b). We briefly summarise the ARKENSTONE-HOT model below, for full details see S24.

ISM material is converted into wind material at a rate of

$$\dot{m}_w = \eta_M \dot{m}_\star, \quad (1)$$

where \dot{m}_\star is the star formation rate (SFR) of the cell, and η_M is the mass loading factor, which is a free parameter that we test in this work. This rate is then stochastically sampled to produce wind particles.

Upon creation, wind particles are given a “launch” energy in addition to the conserved quantities it receives from its parent cell. In contrast to S24, we launch wind particles isotropically, like TNG, with each new particle being given a kick in a random direction. The launch energies correspond to being given a velocity kick with magnitude

$$\Delta v_w = \sqrt{\frac{2\eta_{E,\text{kin}}}{\eta_M} u_\star}, \quad (2)$$

and a specific internal energy of

$$u_w = \frac{\eta_{E,\text{th}}}{\eta_M} u_\star, \quad (3)$$

where $\eta_{E,\text{kin}}$ and $\eta_{E,\text{th}}$ are the kinetic and thermal energy loadings, respectively, that are free parameters we vary in this study. Throughout this paper, we assume that the Mach number of the wind when it is launched is fixed at a value $\mathcal{M} = 1$, which fixes the ratio $\eta_{E,\text{kin}}/\eta_{E,\text{th}} = 5/9$. Like S24, we adopt $u_\star = 5.26 \times 10^5 \text{ (km s}^{-1})^2$ as the characteristic specific energy associated with stellar feedback (dominated by supernovae), which corresponds to one supernova of

10^{51} erg per $95.5 M_\odot$ stellar mass formed (consistent with the value used in Kim et al. 2020a). Unlike EAGLE and TNG, we do not include a metallicity dependence of the energy loading (see Schaye et al. 2015; Pillepich et al. 2018a, for further details of their methods). Additionally, in this first work we take the metallicity of wind particles to be equal to that of the ISM. In reality, the hot, supernova driven phase is expected to have an enhanced metal fraction compared to the ISM (e.g. Li & Bryan 2020; Kim et al. 2020b; Steinwandel et al. 2024a), but we postpone a detailed study of this aspect to future work.

In ARKENSTONE, wind particles are created at a higher mass resolution (i.e. lower mass) than the base resolution of the simulation. This allows for better sampling of the energy injection rate in high specific energy winds, as well as forming part of the cosmological ARKENSTONE-HOT refinement scheme described below. A key result of S24 is that to accurately follow the propagation of a high specific energy wind, a simulation must have sufficient spatial resolution through the sonic point near the base of the wind (defined to be where the outflow velocity passes the radially decreasing sound speed as it adiabatically expands), where material is rapidly accelerated away from the galaxy. ARKENSTONE alleviates some of the difficulties in simulating high specific energy winds by ensuring the spatial resolution in the hot, low density phase of the winds remains a small fraction of the distance to the galaxy, as discussed in Sections 1 and 2.4, thus ensuring we accurately capture the wind’s acceleration. In this work, as in S24, all ARKENSTONE wind particles have a mass 100 times smaller than the base resolution of the simulation (and of the wind particles in the TNG model). We note that the ratio of wind particle mass to base resolution mass was extensively tested in S24, who showed the mass and energy loadings *measured* in idealised simulations were very similar as this input parameter was varied.

After launch, wind particles are recoupled when their host cell has a number density below 10 per cent of the star formation density threshold ($0.1 n_{H,0} \approx 10^{-2} \text{ cm}^{-3}$). We note this is higher than TNG’s threshold of 5 per cent of $n_{H,0}$.

For low energy loading values, the corresponding low launch velocities can sometimes fall below a galaxy’s escape velocity, meaning wind particles are not guaranteed to escape the galaxy. This typically happens in our variable energy loading runs, in the largest haloes in the box. These haloes are regulated by BH feedback anyway – the failure of a supernovae driven wind to escape the galaxy is unsurprising. To prevent wind particles being permanently decoupled, we set a maximum time that a wind particle can exist without recoupling of 100 Myr. If this timer is triggered we return this mass to the ISM, and do not inject the tracer described below to avoid refining star forming material. While the particular choice of a timer of 100 Myr is somewhat arbitrary, we have verified that instead using timer values of 20 and 1000 Myr have no appreciable effect on our results.

2.4 Recoupling and refinement

The key component of the ARKENSTONE-HOT model described in S24 is the introduction of displacement recoupling. This prevents the dilution of the high specific energy of a wind particle, by displacing the existing contents of the host cell to its neighbouring cells before a wind particle recouples. Importantly, this also maintains the existing regular mesh structure so the hydrodynamics scheme continues to work correctly, which would not be the case if the standard AREPO refinement was used. When recoupling occurs, a passive scalar “dye” is injected, which is then advected as a tracer with the hydrodynamics scheme as a conserved quantity. Cells are flagged as “hot wind cells” if the ratio of this quantity to the cell mass, f_w , is greater

Table 1. List of simulation runs presented in this paper, with their wind mass loading, energy loading, and launch velocity. TNG scalings are calculated at $z = 0$ as TNG wind launch velocities have a redshift dependence (Pillepich et al. 2018a); ARKENSTONE values/scalings apply at all redshifts. Note: the scalings with halo mass for TNG and the variable energy loading ARKENSTONE runs are inferred and will actually be scattered about this relation, as both actually scale with the locally measured DM velocity dispersion (and metallicity in the case of TNG).

Run	η_M	η_E	$v_{\text{launch}} [\text{km s}^{-1}]$
TNG	$10.2(M_h/10^{11} M_\odot)^{-5/6}$	(see Fig. 1)	$\max [350, 378(M_h/10^{11} M_\odot)^{1/3}]$
Constant η_E values (Oranges)	0.3	0.1	1061
	0.3	0.3	613
	0.3	0.9	354
Constant η_M values (Pink/Purple)	0.1	0.3	354
	0.3	0.3	613
	0.9	0.3	1061
Varying η_E values (Blues)	0.3	$0.4309(M_h/10^{11} M_\odot)^{-1/6}$	$734(M_h/10^{11} M_\odot)^{-1/12}$
	0.3	$0.4309(M_h/10^{11} M_\odot)^{-1/3}$	$734(M_h/10^{11} M_\odot)^{-1/6}$
	0.3	$0.4309(M_h/10^{11} M_\odot)^{-1/2}$	$734(M_h/10^{11} M_\odot)^{-1/4}$

than a threshold value $f_{w,\text{thresh}}$. In this work this threshold is set as $f_{w,\text{thresh}} = 1000$, the choice of which is described below and was extensively tested. Displacement recoupling only occurs⁴ for host cells that do not already have a high temperature, or those flagged as part of the hot wind. Otherwise, a “simple” recoupling occurs, whereby wind particle quantities are directly injected into its host cell.

Once displacement occurs, the host cell has a lower mass. After recoupling, we wish to prevent this cell from derefining back to the base resolution of the simulation, as high spatial resolution around the sonic point is required to correctly resolve the propagation of a wind (Smith et al. 2024a). We therefore maintain the target mass of hot wind cells at the same mass as the wind particles themselves. This is the refinement scheme that allows ARKENSTONE to successfully resolve the driving of high specific energy winds from close to the galaxy.

However, we do not want to maintain higher resolution in the simulation indefinitely and refine the entire CGM, as this becomes prohibitively expensive. This requires a method of relaxing the refinement as the wind gets further from the galaxy. The fiducial ARKENSTONE implementation was designed and tested in isolated galaxy simulations that had an easily defined frame of reference, making it easy to implement a radial (i.e. galactocentric distance) criterion to prevent lower mass cells from de-refining. However, for the use of the ARKENSTONE model in cosmological simulations, a different method of managing the enhanced resolution is needed, as each galaxy has its own frame of reference. The simplest option could be to use a fixed refinement radius for all galaxies, though given haloes have different sizes this would mean maintaining high resolution for large distances around low mass galaxies, to ensure the same radius also encompasses the sonic point of massive haloes. To do this more efficiently for haloes of different masses therefore requires the wind particles to have knowledge of the halo they are created in.

Our new refinement scheme still makes use of the passive scalar dye injected by wind particles, described earlier, but with the addition of the value decaying over time. The scheme is designed to resolve the base of the galactic wind around galaxies of different masses, and without refining the entire CGM. To do this, we conservatively

aim to maintain high resolution in the wind until $0.1R_{200}$ ⁵ around a given galaxy. The particular choice of $0.1R_{200}$ is somewhat arbitrary, as there is no physical reason for maintaining the resolution to this distance, but the motivations for it are two-fold. Firstly, we cannot easily predict the location of the sonic point around a given galaxy in a cosmological simulation, as it is affected by the galaxy’s geometry and environment. Secondly, the virial radius scales with halo mass, meaning we avoid the issues raised by using a fixed radius. Additionally, an estimate of the virial radius is available from local properties of gas cells that launch wind particles, as described below.

In post-processing of an initial simulation, we verified that the radius of $0.1R_{200}$ comfortably encompasses a hot wind’s sonic point across a wide range of galaxies. There may be more efficient ways of determining a refinement radius, but the current scheme empirically works well without significant additional cost to the simulation.

After wind particles recouple and the dye is injected, we implement an exponential decay of the scalar dye with time,

$$f_w(t + \delta t) = f_w(t) e^{-\frac{\delta t}{t_0}}, \quad (4)$$

where t_0 is a decay constant we set to a fixed $t_0 = 10 \text{ Myr}$. This therefore requires us to change the initial value of the dye, so that by the time the wind reaches $\sim 0.1R_{200}$ the scalar tracer falls below a value of $f_{w,\text{thresh}} = 1000$ and cells are no longer flagged. We emphasise that the specific values of t_0 and $f_{w,\text{thresh}}$ do not matter, it is the combination of them with the current value of the dye that determines a time until a cell begins to derefine. Though we note that using high values of $f_{w,\text{thresh}}$ (together with high values of f_w at recoupling; see below) is preferred so that mixing with pristine, unflagged gas (which can also decrease the dye value) does not significantly affect the timer.

To estimate R_{200} from local properties at launch, we use the 1D dark matter velocity dispersion, which has been found to be correlated with the maximum circular velocity of a halo ($v_{\text{max}} \simeq 1.45\sigma_{\text{DM,1D}}$, Okamoto et al. 2010), and been used in a number of simulations for the launching of winds themselves (e.g. Oppenheimer & Davé 2008; Vogelsberger et al. 2013). It can be shown for a Navarro-Frenk-White (NFW) halo (Navarro et al. 1997) that the maximum circular velocity

⁴ Additional criteria apply that can prevent a cell from displacing material to its neighbours, though these occur rarely. See S24 for details.

⁵ We define R_{200} as the radius within which the mean density is 200 times the critical density of the universe at a given redshift.

v_{\max} can be linked to the virial velocity v_{200} via

$$v_{\max} \approx 0.465 \sqrt{f(c)} v_{200}, \quad (5)$$

where c is the concentration parameter of the NFW halo and

$$f(c) = \frac{c}{\ln(1+c) - c/(1+c)}. \quad (6)$$

R_{200} is then linked to the virial velocity via

$$v_{200} = \sqrt{\frac{GM_{200}}{R_{200}}} = \sqrt{\frac{4\pi G}{3} \Delta_c \rho_{\text{crit}}(z) R_{200}}, \quad (7)$$

where $\Delta_c = 200$ is the overdensity within R_{200} , and $\rho_{\text{crit}}(z) = 3H(z)^2/8\pi G$ is the critical density at the redshift of interest.

Combining equations (5) and (7) with the result of Okamoto et al. (2010) leads to the following relation:

$$R_{200} \approx 3.118 \sqrt{\frac{3}{800\pi G \rho_{\text{crit}}(z) f(c)}} \sigma_{\text{DM, 1D}}. \quad (8)$$

During the simulation we will not know the concentration parameter c for a given halo a priori, so we currently use a fixed value of $c = 5$. Again we emphasise that the specific values entering the calculation do not matter, only the approximate scaling, and we have empirically found this to work.

From the launch quantities defined in Equations (2) and (3), the Bernoulli velocity is given by

$$v_B = \sqrt{v_w^2 + 2\gamma u_w}, \quad (9)$$

which is the characteristic velocity for a wind launched with these properties, and $\gamma = 5/3$ is the adiabatic index of the gas. The initial tracer value given to the wind particles to pass on to their host cell when recoupling occurs is therefore set to be

$$f_{w, \text{init}} = f_{w, \text{thresh}} e^{\frac{0.1 R_{200}}{v_B t_0}}. \quad (10)$$

Gas thus travels approximately $0.1 R_{200}$ before the tracer decays below f_w , so cells maintain a higher resolution within that region. If the value of the tracer carried by a recoupling wind particle is higher than the existing tracer in its host cell, the tracer is overwritten.

Because the mass of wind particles and the cells they recouple into are 100 times smaller than the target cell mass of the base simulation, immediately derefining cells to the base target mass would result in an abrupt jump in mass resolution. To avoid this, we allow a more gradual change in resolution by continuing the decay of the tracer past $f_{w, \text{thresh}}$ until the tracer reaches a new threshold value, which we set in this work to be $f_{w, \text{ref}} = 0.1$. During this time we link the target cell mass directly to the tracer value via

$$m_{\text{target}} = \frac{m_0}{\sqrt{f_w/f_{w, \text{ref}}}}, \quad (11)$$

so that the resolution smoothly degrades until the cell mass reaches the base resolution, m_0 , of the simulation.

2.5 TNG winds

We now summarise the key parts of the TNG wind model (fully described in Pillepich et al. 2018a). As with ARKENSTONE, the TNG wind model also uses hydrodynamically decoupled wind particles (using completely independent implementations), launched isotropically from star forming gas cells. The TNG wind model does not include any of the features that ARKENSTONE uses for resolving high specific energy winds (higher resolution wind particles, displacement recoupling, wind refinement etc.).

Like ARKENSTONE, TNG uses a density threshold for recoupling (5% of the star formation threshold, compared to ARKENSTONE's 10%), at which point the wind particle dumps all of its mass, energy, momentum and metals into its host cell (referred to as simple recoupling in the ARKENSTONE scheme).

Unlike in ARKENSTONE, the wind particles in TNG radiatively cool while hydro-decoupled, with their effective density adopted from the nearest gas cell. We omit this in ARKENSTONE for three reasons. Firstly, for high specific energy winds (which ARKENSTONE-HOT is designed to treat), the density of the local ISM, as measurable in the simulation, is not relevant – we are implicitly assuming that the hot, fast wind is propagating through unresolved low density channels and superbubble breakouts. Secondly, for these hot winds, the radiative cooling time is too long for this additional cooling to be important. Finally, our philosophy with ARKENSTONE is to avoid modelling the evolution of the wind within the ISM as much as possible, instead focusing on the properties of the wind that we source outside of the ISM; radiative cooling while in the ISM could be folded into the input energy loadings if desired.

TNG uses a slightly different parametrisation of input wind properties to our default approach with ARKENSTONE. Instead of choosing the energy and mass content of the wind, with specific energy as a dependent variable, TNG chooses the energy content and velocity of the wind, with mass loading being a dependent variable and thermal energy being a fixed fraction of the kinetic energy. The launch velocity kick scales with the local one-dimensional (1D) DM velocity dispersion, with two modifications – a redshift dependence and a velocity floor – such that the fiducial velocity kick is

$$\Delta v_{w, \text{TNG}} = \max \left[7.4 \times \sigma_{\text{DM, 1D}} \left(\frac{H_0}{H(z)} \right)^{1/3}, 350 \text{ km s}^{-1} \right]. \quad (12)$$

The mass loading is then set as,

$$\eta_M = \frac{2}{v_{w, \text{TNG}}^2} (1 - \tau_w) \eta_E u_\star, \quad (13)$$

where $\tau_w = 0.1$ is the thermal fraction of the wind energy. Note that here we have expressed Equation 13 in a similar parametrisation to our Equations 2 and 3. The combination $u_\star \eta_E$ is equivalent to the quantity e_w in equation 3 of Pillepich et al. (2018a), which has a metallicity dependence (higher wind energy at lower metallicity). Pillepich et al. (2018a) also assumes a SN energy per unit stellar mass formed that is 13% higher than our reference u_\star (relating to minor differences in IMF cutoff masses). Since u_\star and η_E are degenerate as far as the actual wind energy input is concerned (and the difference is slight), for the purpose of comparing energy loadings between ARKENSTONE and TNG on an even footing, we fix u_\star to our value and absorb the difference into the energy loading (along with the metallicity dependence).

2.6 Mass and energy loadings

In this paper we present results from a total of 10 cosmological simulations. In all results we compare to the output of the existing TNG model (but without MHD), ran on the same simulation box. Specifically, we have three runs with a fixed mass loading $\eta_M = 0.3$, and fixed energy loadings of $\eta_E = 0.1, 0.3$, and 0.9 (shown in all plots in shades of orange). This is complemented with three runs with a fixed energy loading $\eta_E = 0.3$, and fixed mass loadings of $\eta_M = 0.1, 0.3$, and 0.9 (shown in pink/purple). We note that the run with $\eta_E = 0.3$ and $\eta_M = 0.9$ catastrophically failed to regulate star formation after $z \sim 0.3$ (see Section 3.5), and became too computationally

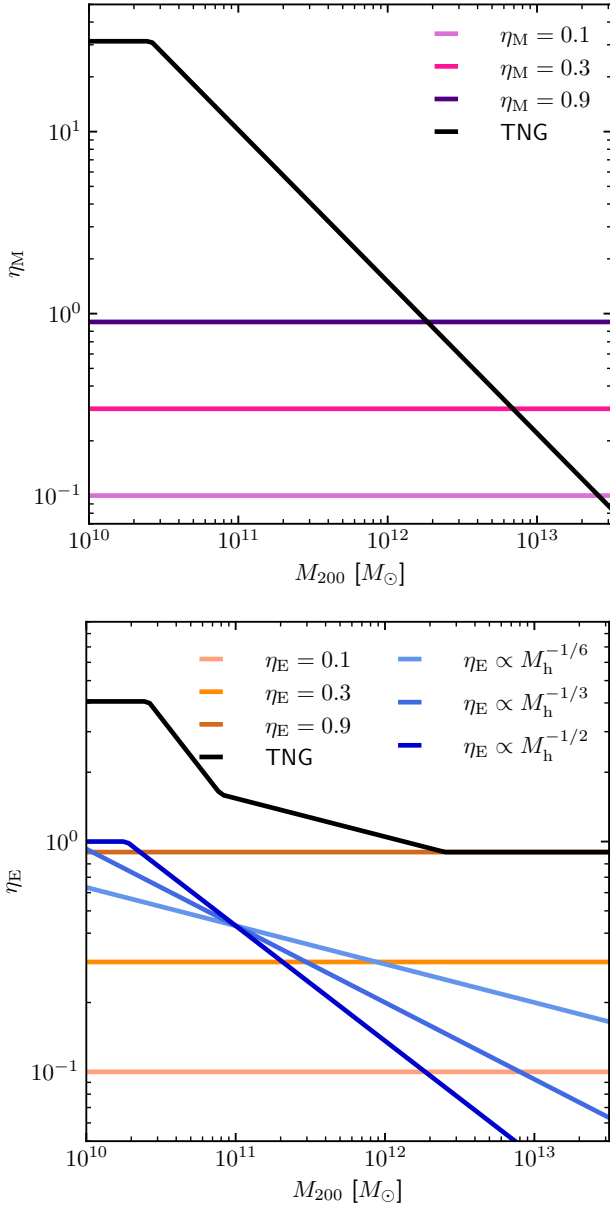


Figure 1. Mass (top panel) and energy (bottom panel) loadings for all ARKENSTONE simulations in this paper, in comparison to scalings from TNG (from the $z = 0$ fits to η_M and v_w in Pillepich et al. 2018a). Both mass and energy loadings in ARKENSTONE runs are generally much lower than in TNG. Throughout most plots in this paper, shades of orange show simulations with constant η_E values and fixed $\eta_M = 0.3$; pink/purple lines show simulations with constant η_M values and fixed $\eta_E = 0.3$; shades of blue show simulations with variable energy loading with a fixed $\eta_M = 0.3$. We note that the input loading values actually applied in the simulations for the latter and TNG have an associated scatter, due to the use of the locally measured DM velocity dispersion (and metallicity in the case of TNG) in their calculation.

expensive to reach $z = 0$. This run is therefore not displayed in figures only showing data from $z = 0$.

Our remaining runs (shown in shades of blue) have a variable energy loading. As discussed in e.g. Carr et al. (2023) and later in this paper, variations in the mass loading of the high specific energy wind do not have as large an impact as variations in energy loading. For these first numerical experiments, we therefore focus only on

variable *energy* loadings. We scale these loadings with the 1D dark matter velocity dispersion, which, as described in the previous section, is linked to the halo mass. These are motivated by findings from previous simulations and semi-analytic models suggesting higher energy loadings are required to regulate low mass galaxies (e.g. Pandya et al. 2021; Carr et al. 2023; Voit et al. 2024b). We characterise this variable energy loading as

$$\eta_E = \eta_{E,\text{norm}} \left(\frac{\sigma_{\text{DM,1D}}}{\sigma_{\text{DM,1D,0}}} \right)^{3\alpha}. \quad (14)$$

The slope α is the expected scaling we wish to realise with halo mass; the additional factor of 3 comes due to the relationship $\sigma_{\text{DM,1D}} \propto M_h^{1/3}$. $\sigma_{\text{DM,1D,0}}$ is the characteristic DM velocity dispersion for a $10^{11} M_\odot$ halo, which we take to be 51 km s^{-1} . At this halo mass we then take the expected energy loading for a $10^{11} M_\odot$ halo to be $\eta_{E,\text{norm}} = 0.4309$ (equivalent to a normalisation of 0.2 for a halo mass of $10^{12} M_\odot$ when $\alpha = -1/3$). Equation (14) is the input energy loading to simulation these variable energy loading simulations, which then approximately follows the halo mass scaling

$$\eta_E = \eta_{E,\text{norm}} \left(\frac{M_h}{10^{11} M_\odot} \right)^\alpha. \quad (15)$$

Our three runs forming the final group still include a fixed mass loading $\eta_M = 0.3$, but include this parametrisation of a variable energy loading with slopes $\alpha = -1/6, -1/3$, and $-1/2$. We cap the energy loading in these simulations at $\eta_{E,\text{max}} = 1$. All runs in this paper and their basic properties are summarised in Table 1.

We show our loadings for both mass (top panel) and energy (bottom panel) in Fig. 1, compared to the input values for TNG (from the fits of Pillepich et al. 2018a). In TNG, the energy loading (dependent on metallicity) and launch velocity (dependent on redshift and with a minimum value of 350 km s^{-1}) are model inputs, and this then sets the mass loading. The values for our variable energy loading simulations and for TNG actually show a scatter around the analytic lines shown in Fig. 1, induced by scatter in the DM velocity dispersion. It is immediately obvious in the top panel that the mass loadings of all ARKENSTONE runs are dramatically smaller than for TNG in low mass galaxies – the central mass loading value used in most ARKENSTONE runs is 5, 34, and even 100 times lower than TNG for haloes of 10^{12} , 10^{11} , and $10^{10} M_\odot$, respectively.

The bottom panel indicates how *energy* loadings are also high in TNG, due to the requirement of launching large amounts of mass out of the galaxy. The lowest energy loading in TNG, reached at high metallicities, is 0.9 – the highest fixed value we study here. Even our variable runs, which are capped at $\eta_E = 1$, still have energy loadings at least 3.6 times lower than TNG for low mass galaxies.

We re-emphasise that while both our mass and energy loadings are generally lower than in TNG, an important change is that the *specific* energy loading, η_E/η_M , is higher. The rest of this paper is dedicated to exploring the implications of this. Drastically reduced amounts of material are thrown out of the ISM in ARKENSTONE simulations compared to TNG. If this is not offset by the prevention of gas joining the ISM in the first-place, galaxies will grow far too massive. As we will see, however, with high specific energy winds and appropriately scaled energy loadings, this does not occur.

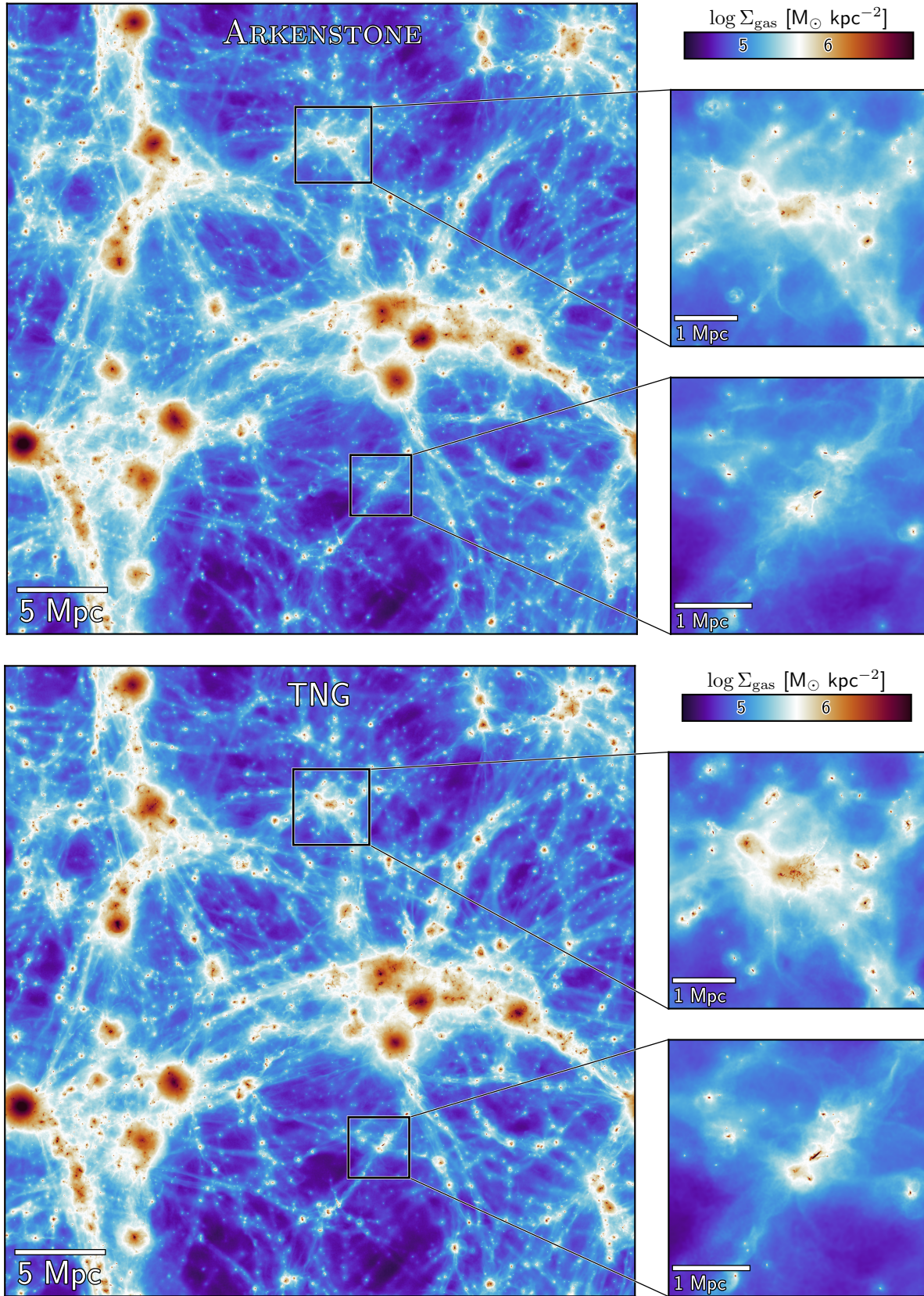


Figure 2. Gas surface density maps of the entire simulation box at $z = 0$ for the ARKENSTONE variable energy loading run with $\eta_E \propto M_h^{-1/3}$ (top panels) and TNG (bottom panels). Zoomed regions highlight two haloes that show particularly different density structures in the two simulations. Gas densities near to galaxies are decreased with ARKENSTONE, with more gas pushed to large distances.

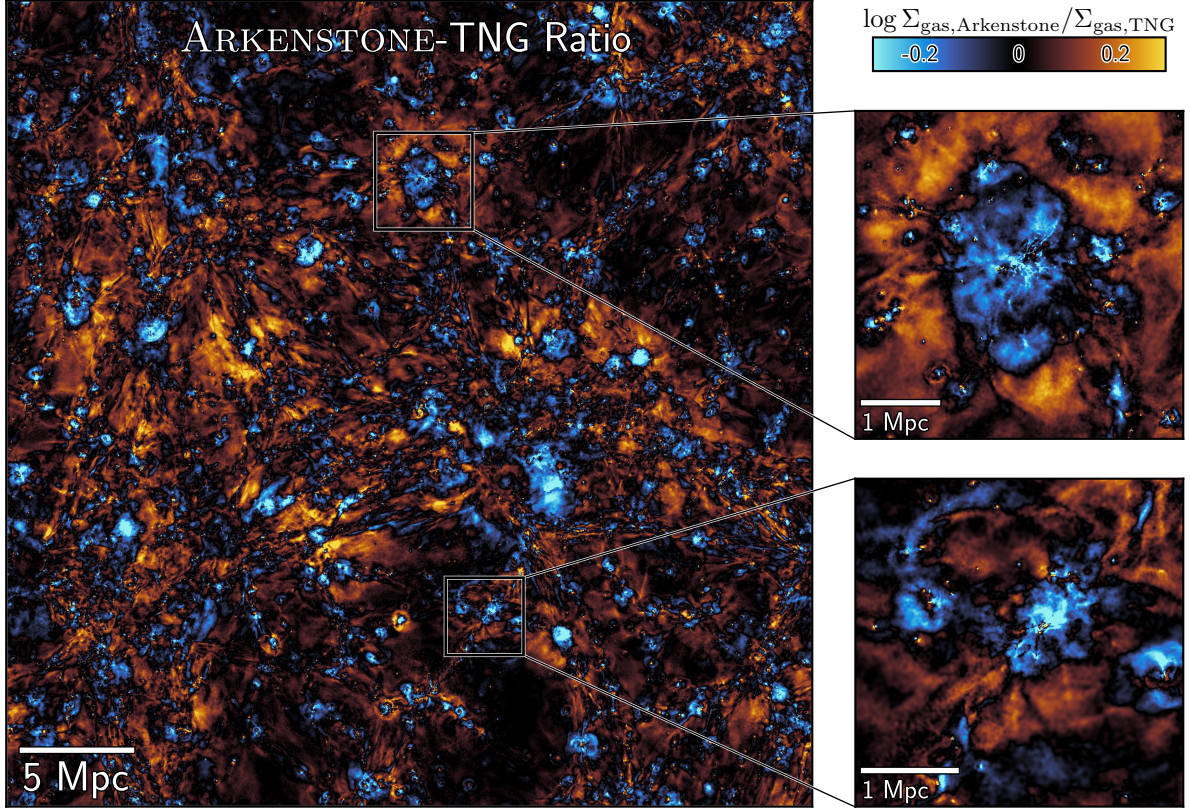


Figure 3. Ratio of the surface density maps shown in Fig. 2, highlighting the differences between the runs. ARKENSTONE has considerably more gas (shown in orange) in the outskirts of haloes and into the IGM, due to winds extending to large distances from central galaxies. Interestingly, within that the CGM sometimes appears somewhat depleted in ARKENSTONE compared to TNG (shown in blue).

3 RESULTS

3.1 First look

In Fig. 2 we show gas surface density maps for the ARKENSTONE simulation with $\eta_E \propto M_h^{-1/3}$ (top panels) and TNG (bottom panels). Orange areas highlight the high gas densities in the centre of haloes, dark blue regions indicate voids. With ARKENSTONE, gas densities close to galaxies are reduced, with a corresponding increase at large radii. This is particularly noticeable in the two haloes highlighted in the zoomed panels on the right, where the dense gas present in TNG is reduced in the ARKENSTONE run.

The differences between the simulations are emphasised in Fig. 3, which shows the ratio of the two maps in Fig. 2. Here, blue regions highlight where the gas surface density is lower in ARKENSTONE than TNG, which occurs close to many galaxies in the simulation volume. Orange regions show where gas surface densities are higher in the ARKENSTONE run, which generally happens on the outskirts of haloes and into the IGM. We note that many of the changes seen in gas density here materialise well outside the virial radii of haloes, affecting the outer CGM and IGM, showing how high specific energy winds can have important impacts far from the galaxies that launch them. Detailed properties of the IGM in ARKENSTONE simulations will be studied in future work, although we note that a generic prediction is a higher IGM gas fraction, potentially in agreement with recent observations (Connor et al. 2024).

3.2 Galaxy properties at $z = 0$

From this Section to Section 3.5, we show a number of population-level results for the properties of galaxies and their gaseous haloes in our simulated boxes. For all plots except the SFR density, solid lines show the median of each quantity, smoothed over the nearest two points for clarity.

In all panels, the solid black line shows the quantity for the TNG model run on the same box. For ARKENSTONE runs, lines with shades of orange show the results for runs with a fixed *mass* loading ($\eta_M = 0.3$) and several constant energy loading values. Shown in pink and purple are runs with a fixed *energy* loading ($\eta_E = 0.3$) and several constant mass loading values. Finally, lines in shades of blue show results for runs with a variable energy loading. Dotted black lines in each panel show observational constraints where available, though we note that a more detailed comparison of full mock observations is deferred to future work.

We further note that due to our limited box size of $(36.9 \text{ Mpc})^3$, our results at high stellar and halo masses are limited by a lack of large objects. For this reason, and the uncertain interplay between ARKENSTONE and the TNG BH model, we suggest caution in interpreting results at these masses. We show individual data points for the largest few haloes in the box (above $M_h \sim 10^{13} M_\odot$), and plot the medians as dashed lines.

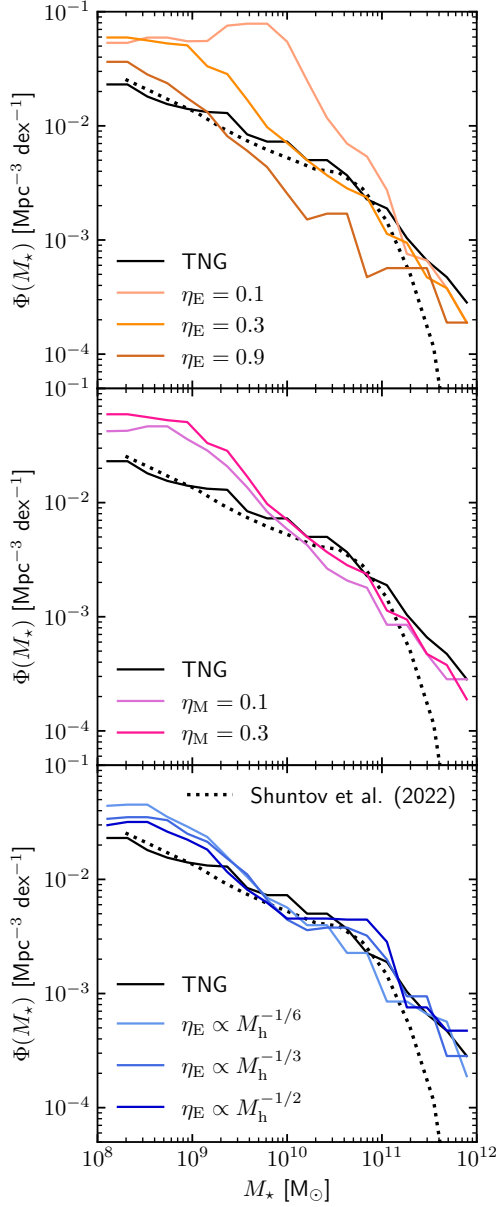


Figure 4. Stellar mass functions at $z = 0$ for simulations with: 1) constant energy loadings and fixed mass loading of $\eta_M = 0.3$ (top panel), 2) constant mass loadings and fixed energy loading of $\eta_E = 0.3$ (middle panel), and 3) simulations with variable energy loading with different slopes α and a fixed mass loading of $\eta_M = 0.3$ (bottom panel). Each panel also shows the result from TNG (black solid line) and observational data (black dotted line) from Shuntov et al. (2022). Lines shown are the median of the data, smoothed over the nearest two bins. For the hot, light winds modelled by ARKENSTONE, energy loading affects the normalisation and slope of the SMF much more than mass loading.

3.2.1 Stellar Mass Functions

Firstly in Fig. 4, we show the SMFs at $z = 0$ for all of our runs. The solid black line in all panels shows the SMF for the TNG model, the parameters of which were tuned to reproduce this quantity. In the top panel, showing effects of changing energy loading while holding mass loading constant, the cumulative feedback effect of energy loading of a hot wind is very clear. The palest line shows the lowest energy loading, $\eta_E = 0.1$, which is evidently ineffective

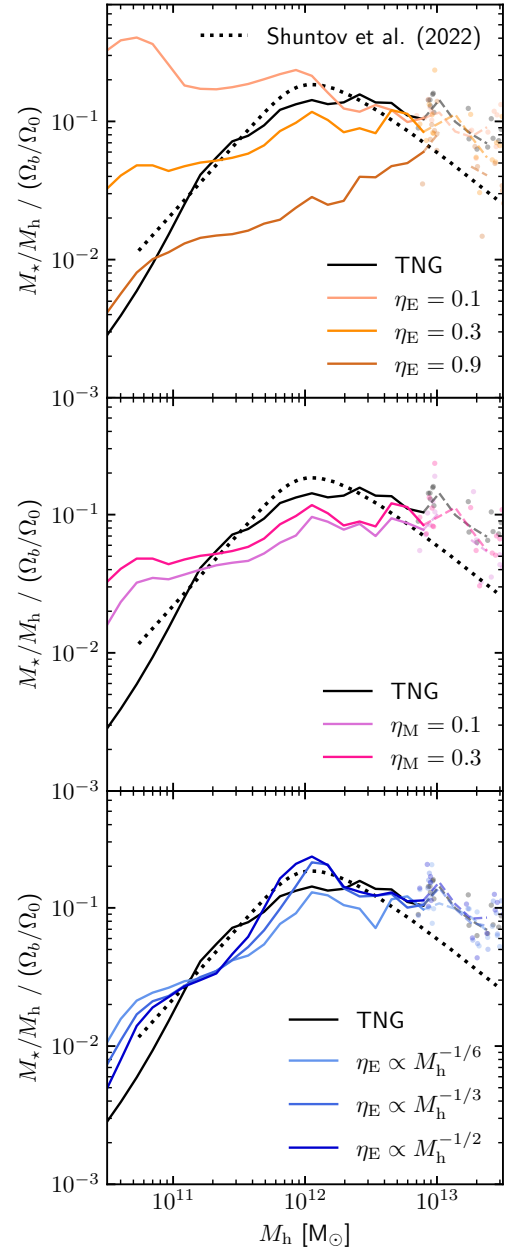


Figure 5. Ratios of stellar mass to halo mass at $z = 0$ as a function of halo mass, normalised by the universal baryon fraction ($f_B = 0.16$, Planck Collaboration et al. 2016). Median lines have the same styles as Fig. 4, with observational data also from Shuntov et al. (2022). For the largest haloes in our box we plot individual scatter points, and change our median lines to be dashed. This is to emphasise that results at high masses should be treated with caution, due to the lack of massive haloes and the dominance of the TNG BH model here. Fixed energy loadings tend to overproduce stars at the low mass end, which can be alleviated by introducing a variable energy loading.

in regulating star formation across a wide range of galaxy masses. The intermediate energy loading of $\eta_E = 0.3$ is shown in the middle orange colour, which brings the SMF down closer to the observations, especially for galaxies at a stellar mass of $\sim 10^{10} M_\odot$. This run still shows an excess of galaxies with $M_* < 10^9 M_\odot$, suggesting a fixed energy loading of 0.3 is not enough to regulate these dwarf galaxies. We discuss this further below. The darkest line in the top panel shows the highest energy loading, $\eta_E = 0.9$, which overregulates star

formation in galaxies with $M_\star > 10^9 M_\odot$, but produces a distribution closer to the observations for $M_\star < 10^9 M_\odot$. This points to the need for a higher energy loading in lower mass systems.

The middle panel of Fig. 4 shows simulations with changes in mass loading for a fixed energy loading of $\eta_E = 0.3$. The effect of these changes in mass loading is much smaller than in energy loading, though the amplitude of the SMF does decrease slightly with decreasing mass loading (i.e. less mass ejection results in less star formation). As we discuss later, this is due to a lower mass loading leading to a hotter, faster wind, resulting in a higher level of preventative feedback due to CGM heating. This is the opposite behaviour to regulation via ejective feedback, where increasing the mass loading tends to lower the star formation by reducing the amount of material in the ISM (as long as there is still enough energy to throw the mass far enough). As a reminder, the run with $\eta_M = 0.9$ (and $\eta_E = 0.3$) completely failed to regulate star formation at low redshifts and did not reach $z = 0$ – this wind has too low a specific energy to provide effective preventative feedback while also having too small a mass loading to act as an efficient source of ejective feedback.

Our runs with an energy loading scaling with halo mass (via the dark matter velocity dispersion) are shown in the bottom panel of Fig. 4. The dependence we have implemented leads to a higher energy loading at lower galaxy masses, which brings the SMF into much better agreement with observations. The slope of the variable energy loading makes a slight difference to the amplitude of the SMF for low mass galaxies, with the steepest value appearing to give the closest match to the observational data.

3.2.2 Stellar Mass Halo Mass Relation

A similar account emerges in the SMHM relation in Fig. 5, here normalised by the cosmic baryon fraction. Recall that this relation was used to calibrate the TNG model. The different (constant) values of energy loading in the top panel show the strong sensitivity of the SMHM to the value of η_E , with the gradient getting steeper with higher energy loading. The lowest energy loading clearly leads to a significant overproduction of stars at the low-mass end, whereas the high-mass end closely follows TNG, likely due to the dominance of the AGN feedback model. An energy loading of 0.3 reduces the stellar mass across all halo masses, most notably below $10^{12} M_\odot$, though there is still an overproduction of stars in the dwarf regime. The highest energy loading of 0.9 dramatically and too effectively reduces the stellar mass of many galaxies – the SMHM relation lies nearly an order of magnitude below the observational data at a Milky Way halo mass of $\sim 10^{12} M_\odot$. Though in the dwarf regime the SMF is closer to the observations, again pointing towards needing higher energy loading in low mass galaxies. Notably, the higher energy loadings also lead to somewhat reduced stellar masses in the largest haloes in our box, though this could be due to the effect of stellar feedback on the growth of BHs and their subsequent feedback.

The mass loading of high specific energy winds can also affect the number of stars formed in lower mass haloes, but much less significantly than energy loading (we note that the gradient of this relation is strongly dependent on energy loading). Lower mass loadings, via hotter, faster winds, lead to less stars forming in lower mass haloes. We note that this ceases to be the case at halo masses above $\sim 10^{12.5} M_\odot$, though as we have discussed, interpretation here is complicated by the AGN feedback.

As with the SMF, having a variable energy loading with halo mass brings the SMHM for ARKENSTONE into better agreement with observations, by further decreasing the stellar masses of low mass haloes. The slope of the variable energy loading directly affects the

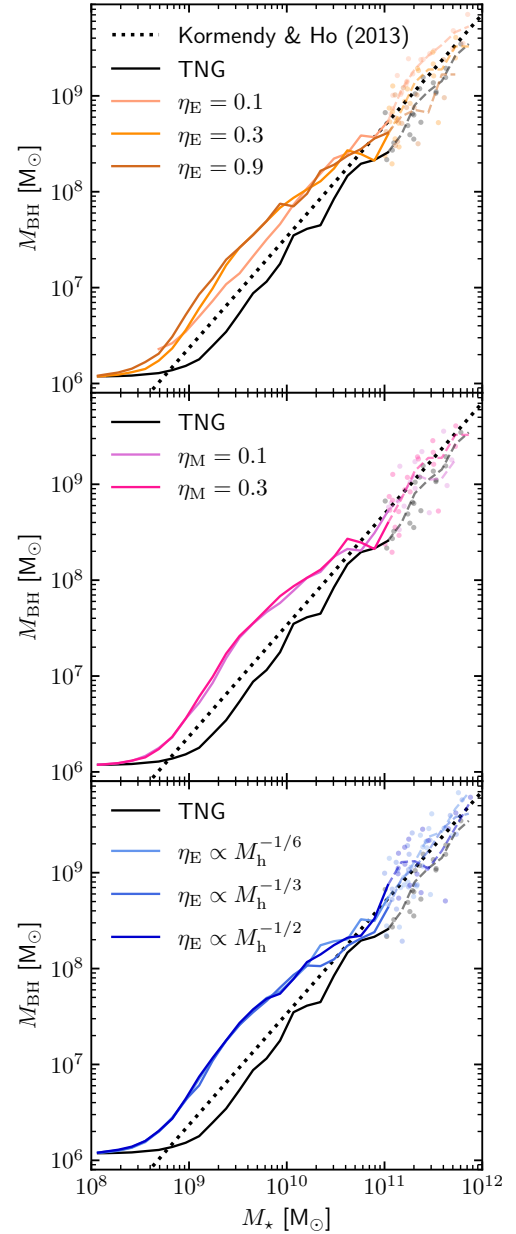


Figure 6. BH-stellar mass relation at $z = 0$. Line and points are displayed in the same way as Fig. 5, with a fit to observational data from Kormendy & Ho (2013) shown as a dotted line. BHs in ARKENSTONE tend to be slightly more massive than in TNG by $z = 0$, likely causing changes in quenching behaviour due to TNG’s feedback model.

slope of the SMHM at low masses, with the steepest relation leading to more suppression below $\sim 10^{11} M_\odot$, and less above that. Our results seem to favour a steeper gradient of η_E , closer to that of Carr et al. (2023) than that of Voit et al. (2024b). At the high mass end, the energy loading becomes small, and so the SMHM relation is set entirely by the TNG BH model.

3.2.3 Stellar Mass Black Hole Mass Relation

Though we have repeatedly discussed the caveats associated with the complex interplay between ARKENSTONE and the fiducial TNG BH model, particularly for galaxies at higher masses, it is still worth look-

ing at how the BH population evolves in these simulations. Therefore, in Fig. 6 we show the stellar mass - black hole mass relation for our simulations. This was another of the observationally motivated relations used to calibrate the TNG model. The inclusion of MHD increases this quantity slightly in the TNG framework, so that the full fiducial TNG model lies slightly *above* the [Kormendy & Ho \(2013\)](#) relation (see [Pillepich et al. 2018a](#)).

In most ARKENSTONE runs, BHs are a factor of a few larger than the equivalent in TNG. Investigating the reasons *why* this happens is beyond the scope of this paper, and will be studied in future work. But we note that none of the parameters for the AGN feedback model used in TNG were changed, despite a dramatic change in how galactic winds work. The larger BHs *do* have implications for galaxy quenching, however, due to the activation of TNG’s powerful kinetic feedback mode having a mass dependent switch (and typically activates in galaxies with stellar masses above of $10^{10.5} M_{\odot}$, [Weinberger et al. 2017](#)).

The only discernible difference in the stellar mass - BH mass relation in our run variations lies at the massive end of the $\eta_E = 0.9$ run, whose black holes tend to lie below the [Kormendy & Ho \(2013\)](#) relation and the other ARKENSTONE runs. This implies that highly energy loaded winds can suppress the growth of black holes in large haloes, though we defer a full investigation of ARKENSTONE in group and cluster-scale haloes to future work.

3.2.4 Galaxy Sizes

Interestingly, we find that the energy loading of our galactic winds plays a strong role in the stellar sizes of galaxies at $z = 0$. In Fig. 7, we show the median 3D stellar half-mass radius as a function of galaxy stellar mass. TNG was calibrated to this metric, though to a different observational dataset than the one presented here. The TNG runs (solid black line) slightly over-estimate the size of galaxies compared to the latest observational data from *JWST* ([van der Wel et al. 2024](#)), though we note that MHD (as present in the original TNG simulations) tends to slightly reduce the size of stellar discs ([Pillepich et al. 2018a](#)). It is also worth noting that the TNG model significantly improved on the over-estimation of galaxy radii found in the original Illustris simulation ([Genel et al. 2018](#)).

With ARKENSTONE, the sizes of galaxies at a given stellar mass has a strong dependence on η_E , with higher energy loadings leading to larger galaxies at nearly all galaxy masses (shown in the top panel of Fig. 7). The central value of $\eta_E = 0.3$ has the best match to the observational galaxy sizes at the low mass end, though we note that the turning point where the slope steepens happens at much lower masses in ARKENSTONE compared to both TNG and observations. This is likely linked to the galaxy becoming quenched by the TNG BH model’s kinetic feedback, which kicks in at slightly lower masses in the ARKENSTONE runs due to larger BH masses. We postpone a more detailed study of the structure of galaxies to future work. The bottom two panels show that galaxy sizes are essentially independent of mass loading, and also change little when including a variable energy loading (with perhaps a slight decrease in galaxy sizes at the massive end, though with few haloes this trend is uncertain).

3.3 CGM properties at $z = 0$

In Fig. 8 we show the median gas fraction within R_{200} , relative to the cosmic baryon fraction, as a function of halo mass. The shape of the TNG line is set by the combination of the stellar and BH feedback models. TNG was also calibrated to this quantity, though data exists

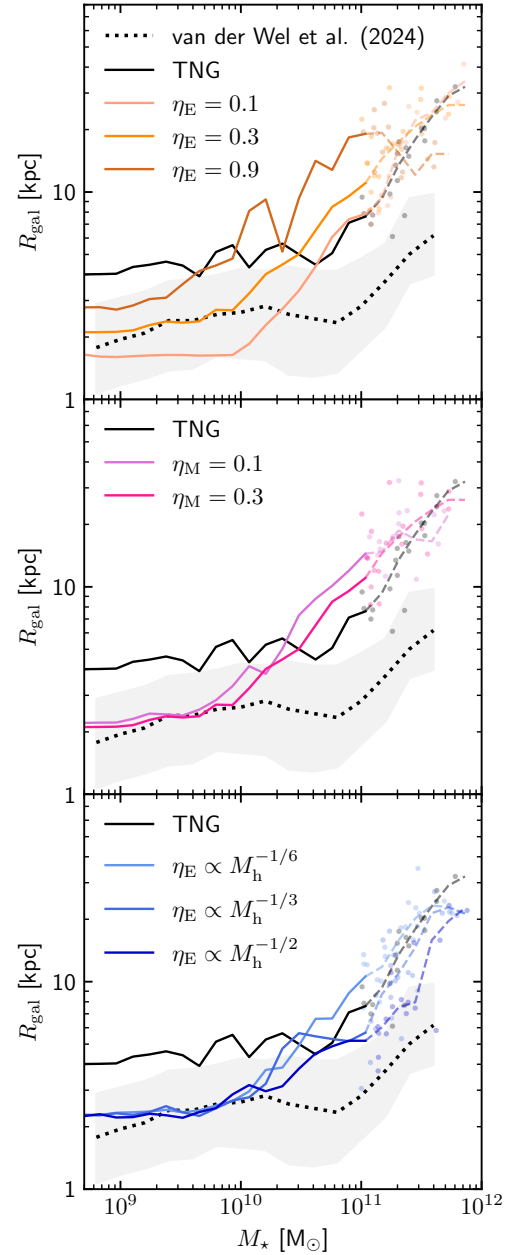


Figure 7. Galaxy sizes at $z = 0$, defined as the stellar half mass radii, as a function of stellar mass. Lines and points are displayed in the same way as Fig. 5, with observational data from [van der Wel et al. \(2024\)](#) included as dotted lines with shaded uncertainty areas. ARKENSTONE tends to produce smaller low-mass galaxies, with the growth of larger galaxies happening at slightly smaller masses than in TNG.

only for groups (of which there are only a handful in our box) and clusters (of which there are none). As this paper focuses on haloes below this scale, where no observational data exists, we do not show comparison data here.

Below a halo mass of $\sim 2 \times 10^{12} M_{\odot}$, the amount of gas in the CGM is regulated by stellar feedback. We have already discussed how TNG tends to rely on ejection of mass from the ISM to regulate star formation. We can see how this ejection also removes much of the CGM at the lowest halo masses, while slightly larger haloes can retain more material. Above $\sim 2 \times 10^{12} M_{\odot}$, the kinetic mode of

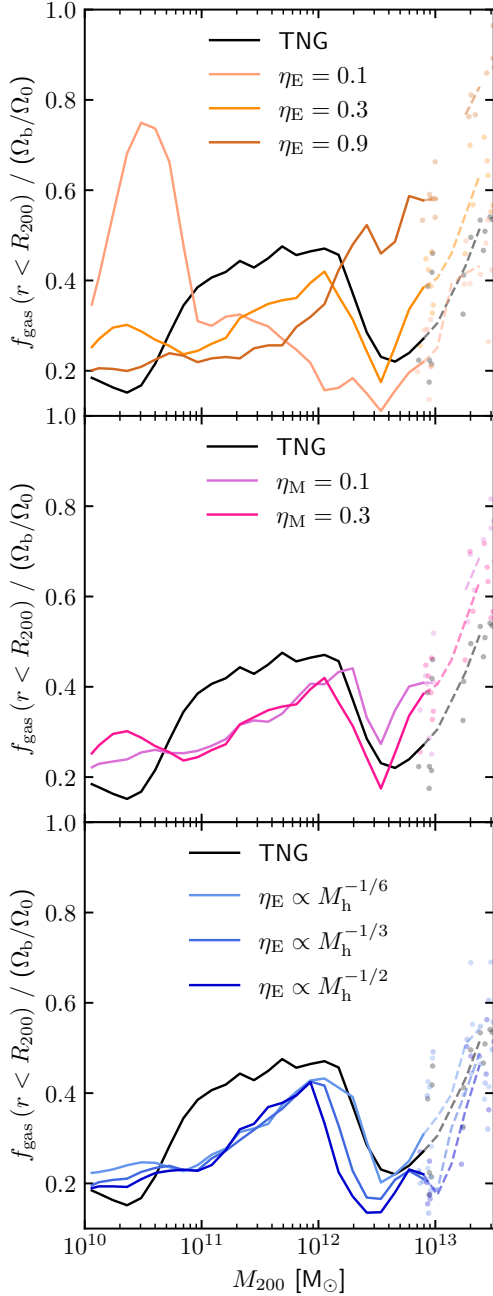


Figure 8. Gas fractions within R_{200} at $z = 0$, normalised by the universal baryon fraction ($f_B = 0.16$, Planck Collaboration et al. 2016). Lines and points are displayed in the same way as Fig. 5. Observational data exists only for the high mass end, which is mostly affected by the TNG BH model, so we do not include it here. Gas fractions at $z = 0$ increase gradually with halo mass for most of the ARKENSTONE simulations, until the kinetic mode of BH feedback begins to act.

TNG’s AGN feedback typically kicks in, expelling much of the inner CGM. As the halo mass increases further, R_{200} increases and haloes can gravitationally hold onto more of that material, leading to an increase in the gas fraction once more.

A number of differences are present between runs with different energy loadings (top panel), with opposing trends either side of a halo mass of $\sim 10^{12} M_\odot$. At low masses, the higher energy loadings lead to more preventative feedback, lowering the gas fraction that ends up

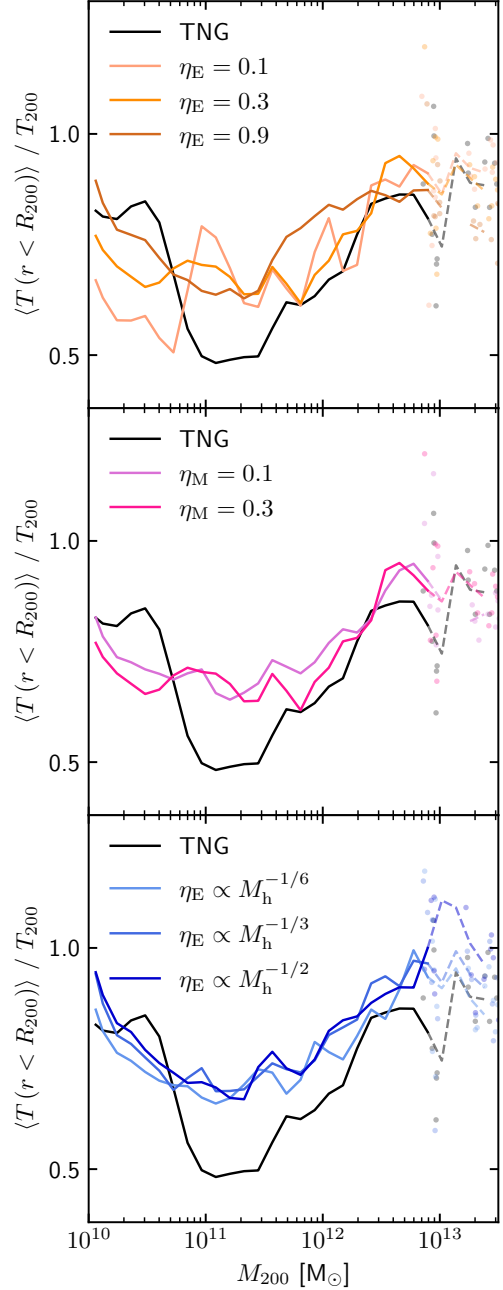


Figure 9. Mass-weighted mean circumgalactic medium temperatures within R_{200} at $z = 0$, normalised by the nominal virial temperature T_{200} . Lines and points are displayed in the same way as in Fig. 5. CGM temperatures as a function of halo mass tend to have a “U”-shape, with a minimum temperature (relative to T_{200}) at halo masses of $\sim 10^{11-11.5} M_\odot$. Temperatures in ARKENSTONE runs tend to lie above those of TNG at $z = 0$.

within R_{200} . At high masses, the highest energy loading actually leads to the retention of more gas. This is likely due to the stunted growth of black holes (see Fig. 6) leading to less feedback, particularly because fewer BHs will then enter TNG’s powerful, mass-dependent kinetic mode. Again, the mass loading of ARKENSTONE winds makes significantly less difference to the fraction of gas within the CGM compared to energy loading. The winds with variable energy loading smooth the abrupt change in median gas fraction present in TNG at halo masses of $\sim 10^{10.5} M_\odot$, and then retain a similar structure at

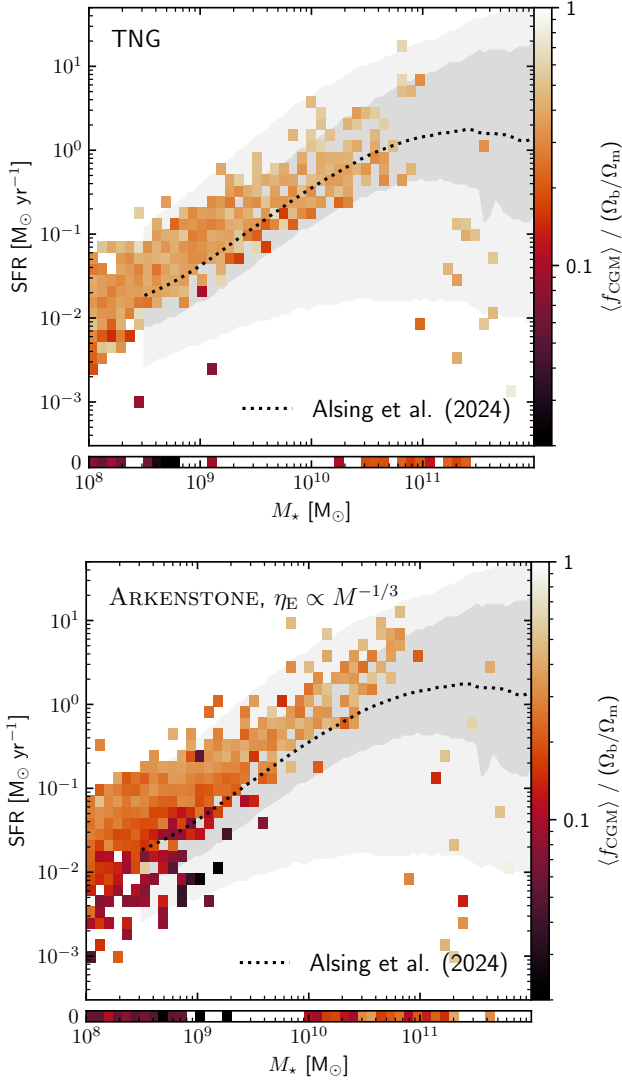


Figure 10. Galaxy SFR as a function of stellar mass at $z = 0$ for TNG (top) and the intermediate variable energy loading ARKENSTONE run ($\eta_E \propto M_h^{-1/3}$, bottom), coloured by the mass-weighted average gas fraction in the CGM (between twice the stellar half mass radius and R_{200}), normalised by the universal baryon fraction. The separated axes at the bottom of each panel show the galaxies with a zero SFR. Observational comparison data is from Alsing et al. (2024), with the median shown by a dotted black line and the inner and outer shaded regions corresponding to the 16 – 84 and 2.5 – 97.5 percentile ranges, respectively. With ARKENSTONE, the SFR in low mass galaxies is correlated with the gas fraction in the CGM – indicative of preventative feedback.

high masses as the AGN feedback acts in the same way. Gas fractions within R_{200} at $z = 0$ in ARKENSTONE tend to lie below those of TNG – this CGM depletion can be seen in the regions close to galaxies in Fig. 3.

Preventative feedback can act through the heating of the CGM (and IGM) around galaxies, inhibiting the cooling of gas onto the central galaxy. To study this, in Fig. 9 we show the mass-weighted temperature of all non-star forming gas cells (those not on the eEoS described in Section 2) within R_{200} , normalised by the halo virial temperature $T_{200} = \mu m_p G M_{200} / (2k_B R_{200})$, where $\mu = 0.59$ is the mean molecular weight of ionised primordial gas.

The vast majority of haloes in all of the runs in Fig. 9 lie below 1,

indicating a sub-virial mean temperature. TNG has CGM temperatures closest to the virial temperature at the lowest and highest masses, with a dip in between at $\sim 10^{11-11.5} M_\odot$. This dip likely corresponds to haloes with a virial temperature near the peak of the cooling curve, leading to more efficient cooling (Fielding et al. 2017), particularly in TNG where the CGM density is higher than in ARKENSTONE (see Fig. 8). Like the gas fraction plot, the relationship at low masses changes more smoothly in ARKENSTONE compared to TNG. The ARKENSTONE runs have a somewhat similar shape, with a minimum in CGM temperature in the halo mass range $\sim 10^{11-11.5} M_\odot$, but with the average $z = 0$ temperature being higher. There are no clear changes between the different ARKENSTONE simulations, with the exception of hotter CGM temperatures for the lowest mass galaxies when fixed energy loadings are increased. We note that this median value of the mass-weighted mean temperatures of haloes hides significant complexity in the CGM, which generally cannot be characterised by a single virial temperature (Lochhaas et al. 2021).

In Fig. 10 we see how this change in CGM properties drives the regulation of star formation. We show two-dimensional histograms of the SFR of galaxies as a function of stellar mass, highlighting the star-forming main sequence for TNG (top panel) and the central variable energy loading ARKENSTONE run (bottom panel). The histogram is coloured by the mass-weighted average CGM gas fraction (defined as the gas within R_{200} minus the gas within twice the stellar half mass radius), normalised by the cosmic baryon fraction. The darker regions therefore indicate where the CGM is relatively depleted of gas, which for ARKENSTONE is interestingly correlated with lower SFR for low mass galaxies. This trend is not present in TNG, which tends to have larger CGM gas fractions in general. The combination of these highlights the preventative nature of feedback with high specific energy winds.

3.4 Preventative feedback in action at $z = 2$

In this section we show a subset of the above results at $z = 2$, where the star formation rate is higher, and so the subsequent feedback is stronger. This allows us to illuminate the differences between how ARKENSTONE and TNG regulate star formation, even though they both can lead to similar $z = 0$ galaxy properties. Note that in this section our plots also include the simulation with fixed $\eta_M = 0.9$ and $\eta_E = 0.3$, which did not reach $z = 0$ and thus was not shown previously.

In Fig. 11 we show the SMHM at $z = 2$, which shows mostly similar trends to $z = 0$. Changing the energy loading of the hot wind has the greatest effect on both the normalisation and (at low and intermediate halo masses) the slope of the SMHM (top panel), with a larger effect shown at smaller halo masses. The mass loading affects the normalisation of the SMHM but not the slope (central panel), with higher stellar masses with higher mass loadings. As discussed earlier, this relationship is due to lower mass loading causing a hotter and faster wind (with the same total power) and increased preventative feedback. The variable energy loadings (bottom panel) counter the overproduction of stars at the low mass end, bringing the SMHM closer to that of TNG. Notably, all of the simulations lie above the observationally inferred SMHM at $z = 2$ from Shuntov et al. (2022).

The most significant differences between the runs, which hold the key to understanding how ARKENSTONE differs from TNG, are shown in the gas fraction (Fig. 12) and temperature (Fig. 13) plots.

Turning first to the gas fractions, for TNG this starts off low at the smallest halo masses, before increasing to ~ 80 per cent of the cosmic baryon fraction at a halo mass of $10^{12} M_\odot$, and slowly declining beyond that as the black hole feedback takes effect. For ARKENSTONE

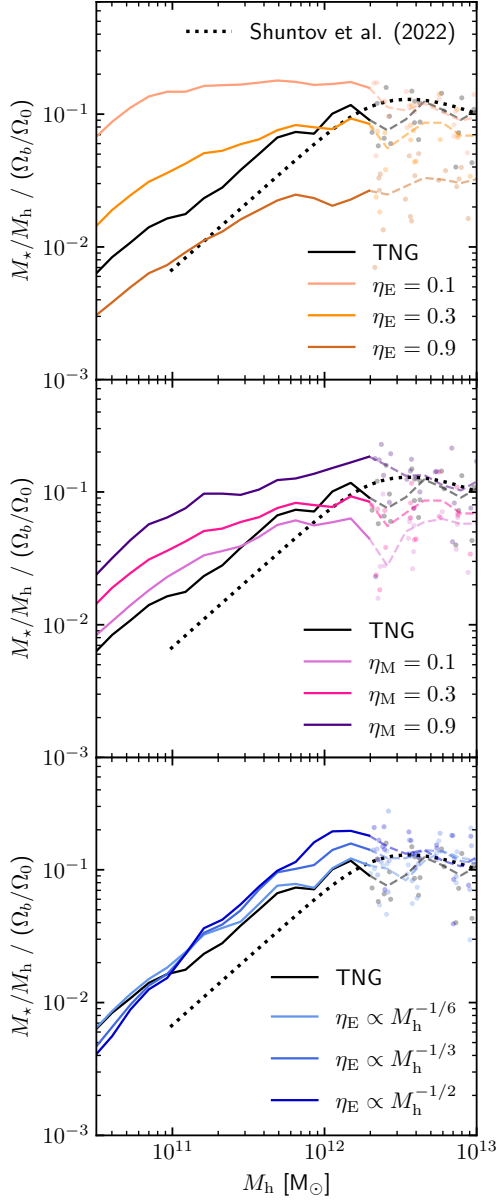


Figure 11. Stellar to halo mass ratios at $z = 2$, normalised by the universal baryon fraction ($f_B = 0.16$, Planck Collaboration et al. 2016). Lines and points are displayed in the same way as Fig. 5, with observational data again from Shuntov et al. (2022). The mass loadings of the hot winds in ARKENSTONE have an impact on the normalisation of the SMHM relation, with lower values leading to less star formation due to a hotter and faster wind.

the gas fraction is much flatter across halo masses. For simulations with different constant energy loading values, the normalisation for haloes below $10^{12} M_\odot$ is inversely proportional to η_E . At the TNG ‘turnover’ mass of $10^{12} M_\odot$, the ARKENSTONE runs have a gas fraction of 40–50 per cent of baryons, around half of TNG’s value at this point. The strong implication of this is that either high specific energy winds push gas outside R_{200} , or gas is prevented from accreting within R_{200} in the first place. This ‘prevention-via-CGM-depletion’ scenario, in contrast to ISM ejection, is a central feature of the ARKENSTONE model. Notably, the relationship between energy loading and gas fraction reverses in haloes above $10^{12} M_\odot$, though this is likely due

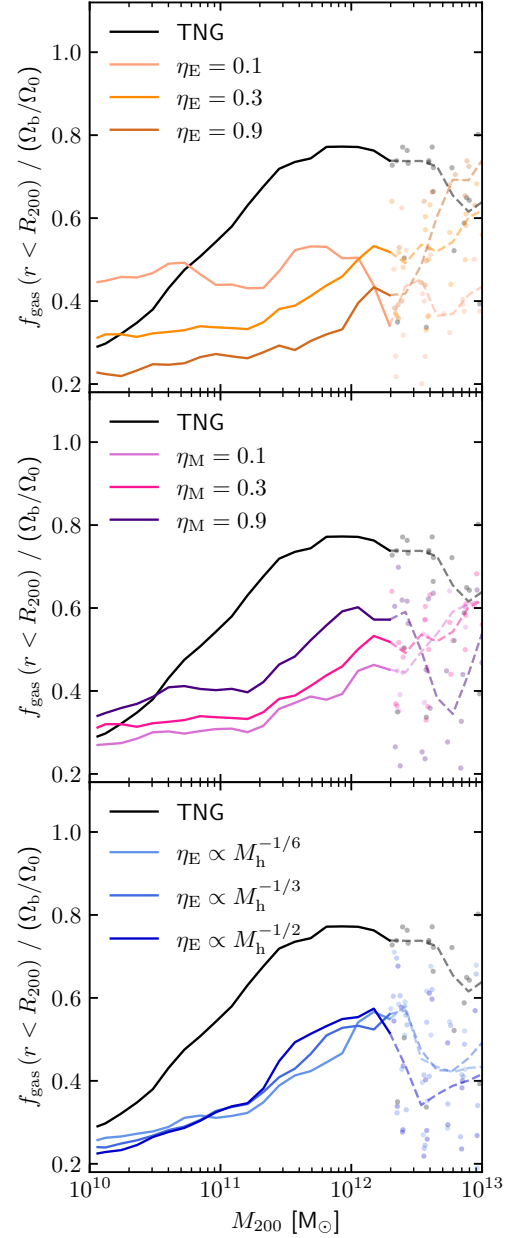


Figure 12. Gas fractions within R_{200} at $z = 2$, normalised by the universal baryon fraction ($f_B = 0.16$, Planck Collaboration et al. 2016). Lines and points are displayed in the same way as in Fig. 5. The amount of gas in the CGM at $z = 2$ is significantly different between ARKENSTONE and TNG. The preventative feedback in ARKENSTONE reduces the amount of gas within the virial radius, lowering inflows onto the central galaxy.

to the variations in stellar feedback affecting black hole growth and feedback.

As we have seen for many of the quantities in this paper, varying the mass loading affects the gas fractions, but has a much smaller impact than variations in energy loading. The lowest mass loading of $\eta_E = 0.1$ has also the lowest gas fractions for low and intermediate mass galaxies, indicating that hotter and faster winds reduce the baryon content of the CGM even more at higher redshift. The variable energy loadings on the other hand lead to a gradually increasing gas fraction as a function of halo mass, up to a halo mass of $\sim 10^{12} M_\odot$.

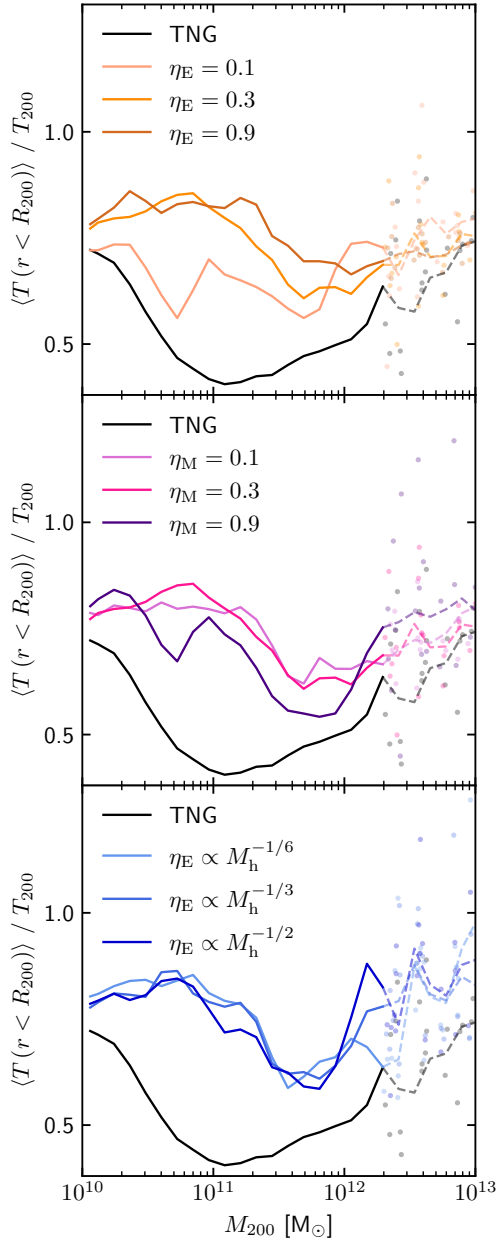


Figure 13. Mass-weighted mean CGM temperatures within R_{200} at $z = 2$, normalised by the nominal virial temperature T_{200} . Lines and points are displayed in the same way as Fig. 5. Like the gas fractions, the CGM temperature is very different between ARKENSTONE and TNG. Variations in energy loading significantly change the mean CGM temperature, with a hotter, more diffuse CGM acting to reduce inflows to the central galaxy.

This slope, and the peak gas fraction value of ~ 50 per cent, are both much smaller than in TNG.

The temperature of the CGM is also an indicator of preventative feedback, with hotter, diffuse gas having longer cooling times and so reducing inflows onto the central galaxy. The CGM temperature at $z = 2$ is shown in Fig. 13, defined in the same way as Fig. 9. Here we again see a strong difference between TNG and ARKENSTONE. The CGM temperatures at the lowest masses considered are largely similar between the runs, but while TNG’s decreases to much cooler temperatures for haloes around $\sim 10^{11} M_{\odot}$, the ARKENSTONE runs stay hotter throughout the entire halo mass range.

The temperature difference varies with energy loading (top panel), particularly in the halo mass range $10^{11-12} M_{\odot}$. Higher energy loading leads to a hotter and more diffuse CGM, more able to prevent gas accreting onto galaxies and forming stars. The highest mass loaded ARKENSTONE run leads to a cooler CGM, as more energy is used to transport a heavier wind. The slope of the variable energy loading does not strongly impact the CGM temperature at $z = 2$.

ACROSS all ARKENSTONE runs, the median CGM temperature at $z = 2$ is nearly always above that of TNG, even in the case of higher mass loadings. Across the parameter space studied in this work, preventative feedback therefore plays much more of a role, with the CGM being consistently hotter and more diffuse.

3.5 Evolution with redshift

To emphasise the differences in redshift evolution between the runs we plot the global star formation rate density (SFRD) versus redshift in Fig. 14. It should be noted that comparison to observations (included for reference) should be made with caution because of the limited box size. However, the relative comparison between simulations remains informative. In these panels, it is clear that cosmic star formation history is most sensitive to the change in energy loading.

In the top panel, with fixed mass loadings of $\eta_M = 0.3$, the run with the lowest energy loading, $\eta_E = 0.1$ has a global SFRD that rises higher than any other run at cosmic noon. And while the higher energy loading runs generally have a declining SFRD to $z = 0$, the lowest energy loading simulation turns up again at low redshift. The ARKENSTONE simulations all tend to have the turnover at cosmic noon occurring slightly earlier than in TNG, though we caution this is dominated by the largest few haloes in the box. These are in turn sensitive to the interaction between stellar feedback and the TNG BH model, which again has not been calibrated and is beyond the scope of this work.

For runs with a fixed energy loading $\eta_E = 0.3$, varying the mass loading of the hot winds also affects the SFRD, though for high and intermediate redshifts the effect is smaller than that of energy loading. Again, lower mass loadings suppress star formation further, due to the wind being hotter and faster (e.g. Voit et al. 2024a). For the case of $\eta_M = 0.9$, the higher mass loading of the wind has disastrous consequences for the regulation of star formation, with the star formation rate rising essentially unchecked after $z = 0.3$. We stop this simulation shortly after this, as the high densities of gas, stars and wind particles lead to a significant increase in computational cost.

The SFRDs for runs with variable energy loading have a different shape to that of TNG, with a suppression of star formation at high redshift, before a rapid increase to cosmic noon. This is due to the higher energy loading for lower halo masses, which suppress star formation at early times. As discussed in Section 4, the tests we have performed in this work have not been calibrated, and are an investigation of how high specific energy winds *alone* can regulate star formation via preventative feedback. To fully explain the presence of the massive early galaxies identified with JWST (e.g. Finkelstein et al. 2024) may require a change in the star formation prescription and possibly a combination of ejective and preventative feedback, which we will study in detail in future work with the full ARKENSTONE model.

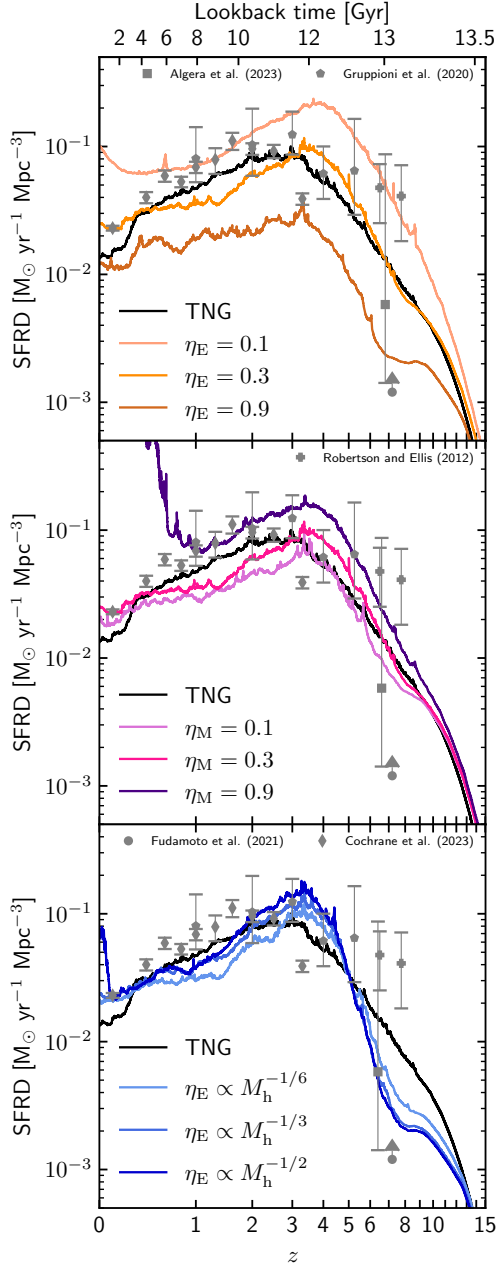


Figure 14. Global star formation rate density at each simulation timestep in our simulated boxes as a function of redshift. Line styles are the same as those in Fig. 5. Observationally inferred data comes from several different methods (Robertson & Ellis 2012; Fudamoto et al. 2021; Gruppioni et al. 2020; Cochrane et al. 2023; Algera et al. 2023). Higher energy loadings can lead to much more suppression in star formation.

4 DISCUSSION

The core result of this paper is that star formation can be regulated by high specific energy winds. Fig. 4 shows this across a wide variety of halo masses using such winds *only* (as a reminder, the cold cloud component of the full ARKENSTONE framework is not active in this paper). This is a significant pivot away from the highly mass loaded winds of many existing cosmological simulations – a shift from primarily ejective towards primarily preventative feedback. The balance between the two has yet to be determined, and will require cosmo-

logical simulations with the full ARKENSTONE model, but we have shown in this work how high mass loadings are *not necessary* to regulate star formation in low and intermediate mass galaxies if sufficient energy is injected into the system via hot winds (controlled by the ratio of energy loading to mass loading). This does not require unphysically large amounts of energy to be injected, indeed we emphasise that ARKENSTONE is green: star formation is regulated while using considerably less energy than existing simulations (see Fig. 1). The important characteristic demonstrated in this work is the high *specific energy* of the wind, further discussed below (and in Voit et al. 2024a,b). Second-order observables, especially of the CGM, will be essential to disentangle the contribution from ejective and preventative feedback in the future.

As discussed in Section 2.6, at $z = 0$ the mass loadings of galaxies at 10^{10} , 10^{11} , and $10^{12} M_{\odot}$ in the TNG model are approximately 31.4, 10.2 and 1.5, respectively. For energy loadings the values are approximately 3.6, 1.36 and 0.93, respectively. Compare these to the fixed $\eta_M = \eta_E = 0.3$ of the central fixed variation of ARKENSTONE or even the variable energy loading run which has a cap at $\eta_{E,\max} = 1$, and we can see a dramatic shift in how galaxies are regulated – much less material enters and leaves the galaxy with ARKENSTONE’s preventative feedback.

Looking further at the gas fractions at $z = 2$, it is clear that the CGM is significantly depleted within R_{200} in the ARKENSTONE runs, considerably more so than in TNG. Interestingly, however, by $z = 0$ the differences between the two are much smaller – much of the ejected material is recaptured by the halo. Despite this, at $z = 0$ there is still a correlation between CGM gas fraction and SFR, as shown in Fig. 10. These results have numerous implications for metal enrichment of the CGM and IGM, and for gas flows since cosmic noon, which will be studied in future work.

In Sections 1 and 2 we motivated our investigation and choices of parameters based on recent analytic and semi-analytic works. The gas-regulator model of Carr et al. (2023) simplifies the baryon cycle to an exchange of mass, metals, and energy between reservoirs of stars, the ISM and the CGM. They find that observables such as the SMHM relation can be reproduced with winds that have low mass loadings and high specific energy. They find that $z = 0$ stellar masses are largely insensitive to changes in mass (and metal) loading, but dependent on energy loading, in good agreement with our results. While the dependence of η_E on halo mass that Carr et al. (2023) finds is needed to reproduce the SMHM is slightly steeper than what we have tested, we find the same general trend of higher η_E at lower halo masses is required. A notable result of Carr et al. (2023) is that highly mass loaded winds tend to lead to a denser CGM with lower specific energy, allowing gas to return to the galaxy on shorter timescales. Our results on the CGM gas fraction and temperature support this, with the high mass loaded winds of TNG generally leading to a cooler, more massive CGM (see Figs. 8, 9, 12, and 13).

Pandya et al. (2023) used a semi-analytic model framework to study CGM evolution and its impact on galaxy evolution, with the additional inclusion of turbulence to act as regulation in addition to thermal energy. Like us, Pandya et al. (2023) finds that the average global CGM temperature does not have to be at the virial temperature (and is in fact often below). They also find higher specific energy winds (with higher η_E/η_M) to lead to a hotter, more turbulent CGM. We do find a similar temperature increase at $z = 2$ (Fig. 13), though the trend is less clear at $z = 0$. Interestingly, with ARKENSTONE the ratio η_E/η_M alone does not set the average CGM temperature, as the runs with $(\eta_E, \eta_M) = (0.9, 0.3)$ and $(0.3, 0.1)$ tend to have slightly different temperatures (with the former being hotter) despite the same

loading ratio. We postpone a detailed study of CGM turbulence to future work.

A key comparison to make is to the minimalist regulator model of [Voit et al. \(2024a,b\)](#), which reduces galaxy evolution and the baryon cycle to three coupled differential equations. ARKENSTONE acts to couple supernova feedback to the CGM. This model predicts that the CGM expands and contracts depending on the comparison between the specific energy of gas injected into the CGM via feedback versus the specific energy it had when accreted. Thus, the minimalist regulator model offers a physical interpretation for many of the results in this paper – high specific energy winds drive the expansion of the CGM, reducing the inflow rate onto central galaxies and the corresponding SFR. This is particularly evident in Fig. 3, which highlights the expanded size of the CGM around many galaxies in our simulated volume. The regulator model also offers an explanation for why our ARKENSTONE simulation with the highest mass loading catastrophically fails at low redshift – a higher η_M at fixed η_E drops the specific energy of the wind, leading to a contracted CGM, more cooling, more recycling of material, and thus a higher SFR. Our simulations provide evidence for the important role of the specific energy of galactic winds in regulating star formation and shaping the properties of the CGM.

5 CONCLUSIONS

In this paper we have demonstrated the use of the new ARKENSTONE galactic wind model in cosmological simulations for the first time. We described the refinement scheme required for the ARKENSTONE-HOT model to work in cosmological simulations, before testing it on a $(36.9 \text{ Mpc})^3$ box. We perform a series of numerical experiments, with both fixed mass and energy loadings and variable energy loadings that scale with DM velocity dispersion (a proxy for halo mass). In this work we do not calibrate our results to observations, we simply explore the impact of changing the loadings. Throughout the paper, we present our results next to the TNG model for reference.

Our key findings are as follows:

- (i) The ARKENSTONE simulations presented in this paper have substantially lower mass and energy loadings in galactic winds compared to the existing TNG model. This increases the specific energy of galactic winds – they become hotter, faster, and lighter.
- (ii) Such winds do not remove large amounts of gas from the ISM of galaxies, but instead regulate star formation by preventing accretion onto galaxies in the first place via the heating, expansion, and depletion of the CGM, particularly at high redshift.
- (iii) The value of energy loading is the key parameter which affects the stellar masses and sizes of galaxies and properties of the CGM, with a much smaller change arising from variations in mass loading – both the total energy injected into the CGM and the specific energy of the wind contribute to these results.
- (iv) With a variable energy loading that increases for lower mass galaxies, ARKENSTONE provides reasonable agreement with observables like the stellar mass-halo mass relation, and does so with a substantially different feedback paradigm to TNG.
- (v) ARKENSTONE can match observed galaxy scaling relations without exceeding the supernovae energy budget *or* the low mass loadings inferred from observations of dwarf galaxy outflows.

Future work with ARKENSTONE will delve further into the new parameter space opened up by the inclusion of detailed modelling of high specific energy winds. An important aspect of the ARKENSTONE-HOT model to be refined further is the metal loading of the hot winds,

which will have a significant impact on observables of the CGM and IGM. Additionally, while in this work we tied wind loadings to halo-scale properties (enabling a simple numerical experiment), in future we will instead base them on local ISM properties (informed by small scale ISM patch simulations), increasing predictive power. Another key advance to be made with ARKENSTONE is the utilisation of the full multiphase wind model ([Smith et al. 2024b](#)) in cosmological volumes, with subgrid cool clouds embedded in the hot wind. Only by using both aspects of the model can we begin to determine the balance between ejective and preventative feedback in galaxy evolution.

ACKNOWLEDGEMENTS

JSB wishes to thank Laura Sommovigo and Rachel Somerville for assembling observational comparison data, and Stephen Thorp and Justin Alsing for sharing data from pop-cosmos ([Alsing et al. 2024](#)). The authors would also like to thank Shy Genel for providing the initial conditions used in these simulations, and Chris Carr and Mark Voit for useful conversations. This work was supported by the Simons Collaboration on “Learning the Universe”. Computations were performed on the HPC systems Iron, at the Flatiron Institute, Orion, at the Max Planck Computing and Data Facility (MPCDF), and Anvil, at Purdue University. The latter was accessed through allocation PHYS240043 from the Advanced Cyberinfrastructure Coordination Ecosystem: Services & Support (ACCESS) program, which is supported by National Science Foundation grants #2138259, #2138286, #2138307, #2137603, and #2138296 ([Song et al. 2022](#); [Boerner et al. 2023](#)). GLB acknowledges support from the NSF (AST-2108470, AST-2307419), NASA TCAN award 80NSSC21K1053, the Simons Foundation. This work made use of the NumPy ([Harris et al. 2020](#)), SciPy ([Virtanen et al. 2020](#)), Matplotlib ([Hunter 2007](#)), and CMasher ([van der Velden 2020](#)) Python packages.

DATA AVAILABILITY

The data used in this work will be shared on reasonable request to the corresponding author.

REFERENCES

- Abruzzo M. W., Fielding D. B., Bryan G. L., 2024, *ApJ*, **966**, 181
- Algera H. S. B., et al., 2023, *MNRAS*, **518**, 6142
- Alsing J., Thorp S., Deger S., Peiris H. V., Leistedt B., Mortlock D., Leja J., 2024, *ApJS*, **274**, 12
- Anglés-Alcázar D., Faucher-Giguère C.-A., Kereš D., Hopkins P. F., Quataert E., Murray N., 2017, *MNRAS*, **470**, 4698
- Ayromlou M., Nelson D., Pillepich A., 2023, *MNRAS*, **524**, 5391
- Bennett J. S., Sijacki D., 2020, *MNRAS*, **499**, 597
- Boerner T. J., Deems S., Furlani T. R., Knuth S. L., Towns J., 2023, in *Practice and Experience in Advanced Research Computing 2023: Computing for the Common Good*. PEARC '23. Association for Computing Machinery, New York, NY, USA, p. 173–176, doi:10.1145/3569951.3597559, <https://doi.org/10.1145/3569951.3597559>
- Bondi H., 1952, *MNRAS*, **112**, 195
- Bondi H., Hoyle F., 1944, *MNRAS*, **104**, 273
- Carr C., Bryan G. L., Fielding D. B., Pandya V., Somerville R. S., 2023, *ApJ*, **949**, 21
- Cen R., 1992, *ApJS*, **78**, 341
- Cochrane R. K., et al., 2023, *MNRAS*, **523**, 6082
- Concas A., et al., 2022, *MNRAS*, **513**, 2535
- Connor L., et al., 2024, *arXiv e-prints*, p. arXiv:2409.16952
- Crain R. A., et al., 2015, *MNRAS*, **450**, 1937

- Dalla Vecchia C., Schaye J., 2012, *MNRAS*, **426**, 140
- Davé R., Thompson R., Hopkins P. F., 2016, *MNRAS*, **462**, 3265
- Davé R., Anglés-Alcázar D., Narayanan D., Li Q., Rafieferantsoa M. H., Appleby S., 2019, *MNRAS*, **486**, 2827
- Davies J. J., Crain R. A., McCarthy I. G., Oppenheimer B. D., Schaye J., Schaller M., McAlpine S., 2019, *MNRAS*, **485**, 3783
- Davies J. J., Crain R. A., Oppenheimer B. D., Schaye J., 2020, *MNRAS*, **491**, 4462
- Davis M., Efstathiou G., Frenk C. S., White S. D. M., 1985, *ApJ*, **292**, 371
- Dolag K., Borgani S., Murante G., Springel V., 2009, *MNRAS*, **399**, 497
- Dubois Y., et al., 2014, *MNRAS*, **444**, 1453
- Faucher-Giguère C.-A., Lidz A., Zaldarriaga M., Hernquist L., 2009, *ApJ*, **703**, 1416
- Faucher-Giguère C.-A., Quataert E., Hopkins P. F., 2013, *MNRAS*, **433**, 1970
- Fielding D., Quataert E., McCourt M., Thompson T. A., 2017, *MNRAS*, **466**, 3810
- Fielding D., Quataert E., Martizzi D., 2018, *MNRAS*, **481**, 3325
- Fielding D. B., et al., 2020, *ApJ*, **903**, 32
- Finkelstein S. L., et al., 2024, *ApJ*, **969**, L2
- Fudamoto Y., et al., 2021, *Nature*, **597**, 489
- Genel S., et al., 2018, *MNRAS*, **474**, 3976
- Gronke M., Oh S. P., 2020, *MNRAS*, **492**, 1970
- Gruppioni C., et al., 2020, *A&A*, **643**, A8
- Guo Y., et al., 2020, *ApJ*, **898**, 26
- Harris C. R., et al., 2020, *Nature*, **585**, 357–362
- Heckman T. M., Best P. N., 2023, *Galaxies*, **11**, 21
- Henden N. A., Puchwein E., Shen S., Sijacki D., 2018, *MNRAS*, **479**, 5385
- Hopkins P. F., Quataert E., Murray N., 2011, *MNRAS*, **417**, 950
- Hopkins P. F., Quataert E., Murray N., 2012, *MNRAS*, **421**, 3522
- Hoyle F., Lyttleton R. A., 1939, *Proceedings of the Cambridge Philosophical Society*, **35**, 405
- Hu C.-Y., 2019, *MNRAS*, **483**, 3363
- Hummels C. B., et al., 2019, *ApJ*, **882**, 156
- Hunter J. D., 2007, *Computing in Science Engineering*, **9**, 90
- Kado-Fong E., et al., 2024, *ApJ*, **966**, 129
- Kannan R., Marinacci F., Simpson C. M., Glover S. C. O., Hernquist L., 2020, *MNRAS*, **491**, 2088
- Katz N., Weinberg D. H., Hernquist L., 1996, *ApJS*, **105**, 19
- Kelly A. J., Jenkins A., Deason A., Fattahi A., Grand R. J. J., Pakmor R., Springel V., Frenk C. S., 2022, *MNRAS*, **514**, 3113
- Kim C.-G., Ostriker E. C., 2018, *ApJ*, **853**, 173
- Kim C.-G., et al., 2020a, *ApJ*, **900**, 61
- Kim C.-G., et al., 2020b, *ApJ*, **903**, L34
- Kormendy J., Ho L. C., 2013, *ARA&A*, **51**, 511
- Krumholz M. R., Burkhardt B., Forbes J. C., Crocker R. M., 2018, *MNRAS*, **477**, 2716
- Li M., Bryan G. L., 2020, *ApJ*, **890**, L30
- Lochhaas C., Tumlinson J., O’Shea B. W., Peebles M. S., Smith B. D., Werk J. K., Augustin R., Simons R. C., 2021, *ApJ*, **922**, 121
- Marasco A., Fraternali F., Lehner N., Howk J. C., 2022, *MNRAS*, **515**, 4176
- Marinacci F., et al., 2018, *MNRAS*, **480**, 5113
- McCarthy I. G., Schaye J., Bird S., Le Brun A. M. C., 2017, *MNRAS*, **465**, 2936
- McCourt M., Oh S. P., O’Leary R., Madigan A.-M., 2018, *MNRAS*, **473**, 5407
- McQuinn K. B. W., van Zee L., Skillman E. D., 2019, *ApJ*, **886**, 74
- Naiman J. P., et al., 2018, *MNRAS*, **477**, 1206
- Navarro J. F., White S. D. M., 1994, *MNRAS*, **267**, 401
- Navarro J. F., Frenk C. S., White S. D. M., 1995, *MNRAS*, **275**, 56
- Navarro J. F., Frenk C. S., White S. D. M., 1997, *ApJ*, **490**, 493
- Nelson D., et al., 2018, *MNRAS*, **475**, 624
- Okamoto T., Frenk C. S., Jenkins A., Theuns T., 2010, *MNRAS*, **406**, 208
- Oppenheimer B. D., Davé R., 2008, *MNRAS*, **387**, 577
- Ostriker E. C., Kim C.-G., 2022, *ApJ*, **936**, 137
- Ostriker E. C., McKee C. F., Leroy A. K., 2010, *ApJ*, **721**, 975
- Pandya V., et al., 2021, *MNRAS*, **508**, 2979
- Pandya V., et al., 2023, *ApJ*, **956**, 118
- Peebles M. S., et al., 2019, *ApJ*, **873**, 129
- Pillepich A., et al., 2018a, *MNRAS*, **473**, 4077
- Pillepich A., et al., 2018b, *MNRAS*, **475**, 648
- Planck Collaboration et al. 2016, *A&A*, **594**, A13
- Prochaska J. X., et al., 2017, *ApJ*, **837**, 169
- Rahmati A., Pawlik A. H., Raičević M., Schaye J., 2013, *MNRAS*, **430**, 2427
- Ramesh R., Nelson D., 2024, *MNRAS*, **528**, 3320
- Rathjen T.-E., Naab T., Walch S., Seifried D., Girichidis P., Wunsch R., 2023, *MNRAS*, **522**, 1843
- Rees M. J., Ostriker J. P., 1977, *MNRAS*, **179**, 541
- Robertson B. E., Ellis R. S., 2012, *ApJ*, **744**, 95
- Rupke D. S. N., 2018, *Galaxies*, **6**, 138
- Schaye J., Dalla Vecchia C., 2008, *MNRAS*, **383**, 1210
- Schaye J., et al., 2015, *MNRAS*, **446**, 521
- Shuntov M., et al., 2022, *A&A*, **664**, A61
- Silk J., 1977, *ApJ*, **211**, 638
- Smith B., Sigurdsson S., Abel T., 2008, *MNRAS*, **385**, 1443
- Smith M. C., Sijacki D., Shen S., 2018, *MNRAS*, **478**, 302
- Smith M. C., Bryan G. L., Somerville R. S., Hu C.-Y., Teyssier R., Burkhardt B., Hernquist L., 2021, *MNRAS*, **506**, 3882
- Smith M. C., et al., 2024a, *MNRAS*, **527**, 1216
- Smith M. C., Fielding D. B., Bryan G. L., Bennett J. S., Kim C.-G., Ostriker E. C., Somerville R. S., 2024b, *arXiv*, **2408.15321**
- Somerville R. S., Davé R., 2015, *ARA&A*, **53**, 51
- Song X. C., et al., 2022, in *Practice and Experience in Advanced Research Computing 2022: Revolutionary: Computing, Connections, You. PEARC ’22. Association for Computing Machinery, New York, NY, USA*, doi:10.1145/3491418.3530766
- Springel V., 2010, *MNRAS*, **401**, 791
- Springel V., 2015, N-GenIC: Cosmological structure initial conditions, Astrophysics Source Code Library, record ascl:1502.003
- Springel V., Hernquist L., 2003, *MNRAS*, **339**, 289
- Springel V., White S. D. M., Tormen G., Kauffmann G., 2001, *MNRAS*, **328**, 726
- Springel V., et al., 2005, *Nature*, **435**, 629
- Springel V., et al., 2018, *MNRAS*, **475**, 676
- Steinwandel U. P., Rennehan D., Orr M. E., Fielding D. B., Kim C.-G., 2024a, *arXiv e-prints*, p. arXiv:2407.14599
- Steinwandel U. P., Kim C.-G., Bryan G. L., Ostriker E. C., Somerville R. S., Fielding D. B., 2024b, *ApJ*, **960**, 100
- Strickland D. K., Heckman T. M., 2009, *ApJ*, **697**, 2030
- Strickland D. K., Stevens I. R., 2000, *MNRAS*, **314**, 511
- Suresh J., Nelson D., Genel S., Rubin K. H. R., Hernquist L., 2019, *MNRAS*, **483**, 4040
- Thompson T. A., Heckman T. M., 2024, *ARA&A*, **62**, 529
- van der Velden E., 2020, *The Journal of Open Source Software*, **5**, 2004
- van der Wel A., et al., 2024, *ApJ*, **960**, 53
- van de Voort F., Springel V., Mandelker N., van den Bosch F. C., Pakmor R., 2019, *MNRAS*, **482**, L85
- Virtanen P., et al., 2020, *Nature Methods*, **17**, 261
- Vogelsberger M., Genel S., Sijacki D., Torrey P., Springel V., Hernquist L., 2013, *MNRAS*, **436**, 3031
- Voit G. M., Pandya V., Fielding D. B., Bryan G. L., Carr C., Donahue M., Oppenheimer B. D., Somerville R. S., 2024a, *arXiv e-prints*, p. arXiv:2406.07631
- Voit G. M., Carr C., Fielding D. B., Pandya V., Bryan G. L., Donahue M., Oppenheimer B. D., Somerville R. S., 2024b, *arXiv e-prints*, p. arXiv:2406.07632
- Weinberger R., et al., 2017, *MNRAS*, **465**, 3291
- White S. D. M., Frenk C. S., 1991, *ApJ*, **379**, 52
- White S. D. M., Rees M. J., 1978, *MNRAS*, **183**, 341
- Wiersma R. P. C., Schaye J., Smith B. D., 2009, *MNRAS*, **393**, 99
- Wright R. J., Somerville R. S., Lagos C. d. P., Schaller M., Davé R., Anglés-Alcázar D., Genel S., 2024, *MNRAS*, **532**, 3417
- Zabl J., et al., 2021, *MNRAS*, **507**, 4294

This paper has been typeset from a \LaTeX file prepared by the author.